Accepted Manuscript

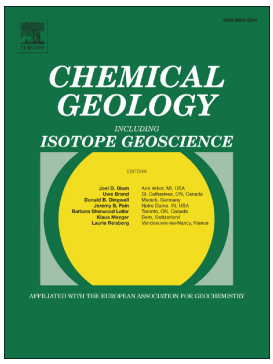


# The effect of fluorine and chlorine on trace element partitioning between apatite and sediment melt at subduction zone conditions

Huijuan Li, Jörg Hermann

PII: S0009-2541(17)30571-5
DOI: doi:10.1016/j.chemgeo.2017.10.016
Reference: CHEMGE 18505

To appear in: *Chemical Geology*

Received date: 1 June 2017
Revised date: 11 September 2017
Accepted date: 10 October 2017

Please cite this article as: Huijuan Li, Jörg Hermann , The effect of fluorine and chlorine on trace element partitioning between apatite and sediment melt at subduction zone conditions. The address for the corresponding author was captured as affiliation for all authors. Please check if appropriate. Chemge(2017), doi:10.1016/j.chemgeo.2017.10.016

# The effect of fluorine and chlorine on trace element partitioning between apatite and sediment melt at subduction zone conditions

**Huijuan Li[1*] and Jörg Hermann[1,2]**

[1] Research School of Earth Sciences, Building 142, Mills Road, The Australian National University, Canberra, ACT 2601 Australia;

[2] Institute of Geological Sciences, Universität Bern, 3012 Switzerland

[*] Corresponding Author: huijuan.li@anu.edu.au

**Abstract**

The effect of F and Cl on trace element recycling during subduction-related sediment melting has been investigated by performing piston-cylinder experiments with a hydrous experimental pelite starting material (EPSM) with variable Cl (~0, 500, 1000, 2000, or 3000 ppm) and F (~0, 700, or 1500 ppm) concentrations, at 2.5 GPa, 800°C. The variations of trace element concentrations in melt are systematically correlated with the variation of F (0.07-0.39 wt%) and Cl (0.07-0.39 wt%) contents. Trace elements Zn, V and Pb, and major elements Fe, Mg and Ca, show positive correlations with each other, and also with the Cl content in melt. The concentrations of light and medium rare earth elements (LMREE) increase with the Cl content in melt, whereas both F and Cl cause a decrease in the concentrations of high field strength elements (HFSE, such as Nb, Ta, Zr and Hf). Trace element (REE, Y, Sr, Th, U) concentrations in apatite are found to increase with the mole fraction of chlorapatite (ClAp). The preference for ClAp is stronger for cations with higher charge (e.g., $Th^{4+}$, $U^{4+}$ > $REE^{3+}$) and larger ionic radii (e.g., LREE > HREE).

Trace element partition coefficients between apatite and melt show up to 4 times variation between experiments, e.g., $D_{La}^{Ap\text{-}melt}$ = 77-281; $D_{Sm}^{Ap\text{-}melt}$ = 176-519; $D_{Sr}^{Ap\text{-}melt}$ = 4-12 and $D_{Th,U}^{Ap\text{-}melt}$ = 4-19. The REE partition coefficients between apatite and melt ($D_{REE}^{Ap\text{-}melt}$) display a concave pattern with the peak at Sm/Nd and a negative Eu anomaly, and are

significantly higher than previously reported values for partitioning experiments conducted at lower pressures and higher temperatures. The high values of $D_{LREE}^{Ap\text{-}melt}$ demonstrate the importance of apatite in terms of LREE partitioning during sediment melting, while allanite/monazite still dominates the partitioning of Th. In the absence of allanite/monazite, apatite-buffered melt is characterized by a significant enrichment of Th relative to La. Because of the contrasting behavior of LREE and HFSE in melt with the addition of Cl and F, the fractionation of these elements in slab-derived sediment melts will be enhanced by the presence of halogens.

**Keywords**: Apatite; Chlorine; Fluorine; Melt; Partitioning; Trace element recycling

## 1 Introduction

Arc basalts display distinctive trace element signatures that include marked enrichment of Pb, large ion lithophile elements (LILE) and light rare earth elements (LREE) relative to high field strength elements (HFSE) and heavy rare earth elements (HREE). Many of these elements are not significantly fractionated from each other during mantle melting and subsequent differentiation. Therefore, their variable enrichment in arcs has been taken to reflect the addition of a subduction component (Hawkesworth et al., 1993; Stolper and Newman, 1994). The $^{10}$Be/Be ratio, Nd, Sr, Pb isotopic compositions of arc magmas (Hawkesworth et al., 1993) and correlations between the chemical characteristics of subducted sediment and arc volcanics (Plank and Langmuir, 1993), all provide definitive evidence of a sediment contribution to arc volcanism. There is increasing evidence that the aqueous fluids formed by dehydration of subducted slab are dilute in both major and trace elements (Green and Adam, 2003; Kessel et al., 2005; Manning, 2004; Spandler et al., 2007), therefore sediment melt may act as the primary agent for transporting incompatible elements from the slab to the mantle wedge (Hermann and Rubatto, 2009; Hermann and Spandler, 2008; Klimm et al., 2008; Plank et al., 2009).

A considerable number of experimental studies have investigated sediment melting at subduction zone conditions (Auzanneau et al., 2006; Hermann and Rubatto, 2009; Hermann and Spandler, 2008; Li and Hermann, 2015; Mann and Schmidt, 2015; Nichols et al., 1994; Schmidt, 2015; Schmidt et al., 2004; Skora and Blundy, 2010; Skora et al., 2015; Spandler et al., 2010; Thomsen and Schmidt, 2008; Tsuno and Dasgupta, 2012, 2011). However, only a few previous studies (Li and Hermann, 2017, 2015; Nichols et al., 1994) involved sediment compositions containing F and Cl. The addition of F and Cl has been shown to enhance trace element partitioning into aqueous fluids (Antignano and Manning, 2008; Bali et al., 2012, 2011; Bernini et al., 2013; Brenan et al., 1995; Keppler, 1996; Rapp et al., 2010; Schmidt et al., 2007; Tanis et al., 2016; Tropper et al., 2011, 2013; Tsay et al., 2017, 2014). However, to date, there have been no experimental investigations into the F and Cl effect on trace element uptake in sediment melt.

To address this question, we have examined the trace element compositions of melt produced by F, Cl-doped sediment melting at fixed *PT* conditions of 2.5 GPa, 800°C. We also report the F and Cl effect on both trace element compositions of apatite and the resultant partition coefficients between apatite and melt. Implications in regard to the role of apatite during trace element recycling within subduction zones are also discussed. Apatite has been recognized as the major host for Phosphorous; however, discussions regarding LREE and Th recycling have focused primarily on the role of monazite (Hermann and Rubatto, 2009; Plank, 2005; Skora and Blundy, 2012; Stepanov et al., 2012) and allanite (Hermann and Rubatto, 2009; Hermann, 2002; Klimm et al., 2008). Apatite can also contain a significant amount of LREE, moreover, it is a ubiquitous accessory mineral in subducted lithologies (e.g., Spandler et al., 2003), and stable over a wide range of *PT* conditions (up to 7.5 GPa in subduction zones, Konzett and Frost, 2009). Therefore, knowledge of LREE partitioning between apatite and fluid/melt in subduction zone settings provides additional constraints on LREE recycling.

## 2 Methods

The set of experiments selected for this study has been previously reported in Li and Hermann (2017, 2015), in regards to F and Cl partitioning between apatite and melt. F, Cl and major element compositions for melt and apatite are listed in Appendix Tables A.1 and A.2 for easy reference. For details of major element analytical methods, please refer to the two publications mentioned above, whereas the experimental, analytical and theoretical methods outlined below focus primarily on the study of trace elements in melt and apatite.

### 2.1 Starting material

A synthetic experimental pelite starting material (EPSM, Table 1), which has a composition similar to both the average composition of "Global Subducting Sediment" (GLOSS, Plank and Langmuir, 1998) and upper continental crust (Rudnick and Gao, 2003), was used to produce sediment melts at 2.5 GPa, 800°C. The staring compositions (EPSM-1-10, Table 2) have the same major element and $H_2O$ contents, but variable Cl (~0, 500, 1000, 2000, or 3000 ppm) and F (~0, 700, or 1500 ppm) concentrations. The lower end of the bulk Cl range (~1.6% NaCleq for EPSM-4, 6) is comparable to the salinity of fluid produced by high-pressure antigorite breakdown (0.4-2 wt% NaCleq, Scambelluri et al., 2004), while lower bulk F contents (~700 ppm) are similar to those of the upper continental crust (e.g., 557 ppm, Rudnick and Gao, 2003). The high end for bulk Cl (~6.4% NaCleq for EPSM-8) is well within the range reported for arc magmas, e.g., 1-10% NaCleq (Wallace, 2005).

The "sol-gel" method was used to produce a trace element-doped $SiO_2$ gel by mixing trace elements in the form of nitrate solutions into tetraethyl orthosilicate [$Si(C_2H_5O)_4$]. The $SiO_2$ gel was then combined with reagent grade oxides, carbonates and phosphates, and the mixture was devolatilized at 1000°C. F, Cl and $H_2O$-bearing intermediate starting compositions were prepared by adding synthetic fayalite, $Al(OH)_3$, NaCl and $CaF_2$ to the sintered mixture as the source of Fe, $H_2O$, Cl and F, respectively. EPSM-1-10 with variable F and Cl contents, were produced by blending F, Cl and $H_2O$-bearing intermediate starting compositions at various ratios. The actual trace element concentrations in EPSM were determined by analyzing a

sintered mixture prepared for one of the intermediate starting compositions. This sintered mixture does not contain Al, Fe or volatiles and has a $SiO_2$ content of 81.4 wt%. It was fused at 1500°C in a box furnace for a few minutes and quenched to glass, then analyzed for trace element contents by LA-ICPMS. As trace elements were added to the silica gel, the ratio of trace element concentration to $SiO_2$ content is constant among all starting compositions. The trace element compositions of EPSM were subsequently calculated based on the $SiO_2$ content of 64 wt% (Table 1). The resultant bulk Pb content (18±9.7 ppm) is significantly lower than expected, which may be due to Pb loss during the fusion process. The actual bulk Pb content is estimated to be 50±10 ppm based on the Pb concentrations in melt and the assumption that Pb and Sr have similar incompatibility.

### 2.2 Experimental techniques

All experiments were performed using a piston-cylinder apparatus employing a 1.27 cm bore pressure vessel. The experimental assembly was comprised of a 2.3 mm diameter gold capsule held within an MgO sleeve, followed by a graphite heater, salt sleeve and an outer Teflon film. Such an experimental assembly has an intrinsic oxygen fugacity close to the Ni-NiO buffer. Previous experiments using the same assembly at similar *PT* conditions (Hermann and Spandler, 2008; Rubatto and Hermann, 2007) have demonstrated that less than 5% of total Fe in garnet is $Fe^{3+}$ (based on stoichiometry analysis), i.e., >90% of the bulk Fe remains as $Fe^{2+}$. As such, we anticipate that the dominant oxidation states for Ce and U are $Ce^{3+}$ and $U^{4+}$, respectively, and Eu occurs as both $Eu^{2+}$ and $Eu^{3+}$. Calculations using the model of Kress and Carmichael (1991) result in an estimate of $Fe^{3+}/Fe^{2+}$ ≈0.2 for melt compositions in this study. Temperatures were monitored using type-B thermocouples ($Pt_{94}Rh_6/Pt_{70}Rh_{30}$) providing an accuracy of ±10°C. Pressures were converted directly from load and are accurate to 0.1 GPa. Rapid quenching was performed by cutting power to the experiments. At *PT* conditions of 2.5 GPa and 800°C, melting of a hydrous EPSM composition with ~7 wt% $H_2O$ produces a high melt fraction of ~50%, with melt quenching into bubble-free glasses (Fig. 1).

### 2.3 Analytical techniques

The trace element composition of melt was determined by LA-ICPMS analysis at the Australian National University, with a pulsed 193 nm ArF Excimer laser (50 mJ output energy at a repetition rate of 5 Hz) (Eggins et al., 1998) coupled to an Agilent 7500 quadrupole ICP-MS. For each time-resolved analysis, we acquired 20s of background (laser off) and 40s of sample signal (laser on). To correct for instrumental drift, standards were analyzed before and after every 10-12 data points. A synthetic glass (NIST 610) was used for external calibration with reference values taken from Pearce et al. (1997). A BCR-2G glass was used as the secondary standard, with the measured compositions given in Table 2 along with reference values from Jochum and Nohl (2008). The $SiO_2$ content of melt determined with SEM EDS analysis was used as an internal standard to correct for the difference in ablation efficiency between the external standard and the sample.

An average of 10-12 data points were collected for each sample, and were closely monitored for contamination from mineral phases, in particular, accessory rutile and apatite with grain sizes of 1-5 μm (Fig. 1). Trace element analyses for melt reported in Table 2 are the averages of data points showing no signs of contamination. Since direct LA-ICPMS analysis of apatite is impractical due to its small grain size, the trace element compositions in apatite were derived from mixed analyses of melt and apatite. The concentrations of REE, Y, Th, U and Sr from analyses with various melt and apatite mixing ratios were plotted against the P concentration. Linear correlations were established with the slope representing the ratio between the given trace element and P content in apatite. Trace element concentrations in apatite were then calculated based on these ratios and the P content in apatite (17.5 wt%). Examples of this regression method are given in Fig. 2. This method has been previously developed, tested and successfully applied to derive trace element compositions for zircon (Rubatto and Hermann, 2007) and monazite (Stepanov et al., 2012) and is applicable to elements that are moderately to highly compatible in apatite. For REE, Y, Th and U, only

regressed values with $R^2$ higher than 0.70 are reported; while the cut-off for Sr was set at $R^2$>0.60.

### 2.4 Theoretical analysis

The aim of this study is to isolate the F and Cl effect on trace element concentrations in melt, from other controlling factors, e.g., the degree of melting, mineral fraction and variations in mineral composition. To illustrate, a mass balance equation based on the partition coefficient of trace element *i*, $D_i^{\text{min-melt}}$ can be written as:

$$D_i^{\text{min-melt}} \times C_i^{\text{melt}} \times X_{\text{min}} + C_i^{\text{melt}} \times X_{\text{melt}} = C_i^{\text{bulk}} \quad (1)$$

where $C_i^{\text{melt}}$ is the concentration of trace element *i* in melt, $C_i^{\text{bulk}}$ is the bulk content of *i*, $X_{\text{min}}$ and $X_{\text{melt}}$ are the mass fractions of mineral and melt, respectively. Expressions for $C_i^{\text{melt}}$ and normalized concentration ($C_i^{\text{melt}}$/ $C_i^{\text{bulk}}$) can be derived from equation (1):

$$C_i^{\text{melt}} = \frac{C_i^{\text{bulk}}}{D_i^{\text{min-melt}} \times X_{\text{min}} + X_{\text{melt}}} \quad (2)$$

$$\frac{C_i^{\text{melt}}}{C_i^{\text{bulk}}} = \frac{1}{D_i^{\text{min-melt}} \times X_{\text{min}} + X_{\text{melt}}} \quad (3)$$

The F and Cl effects on trace element *i* in mineral and melt, are reflected in the variation of activity coefficients for the corresponding *i* component in the mineral and melt phase, which then results in the variation of $D_i^{\text{min-melt}}$. For highly incompatible elements (e.g., Sr and Cs), the values of $D_i^{\text{min-melt}}$ are small in comparison to the value of $X_{\text{melt}}$, therefore $X_{\text{melt}}$ is the dominant controlling factor. For highly compatible elements, i.e., $D_i^{\text{min-melt}} >> X_{\text{melt}}$, $X_{\text{melt}}$ has less importance; concentrations of these elements in melt are determined by the variation of $D_i^{\text{min-melt}}$. For anhydrous mineral phases, e.g., rutile (the major host for Nb, Ta), zircon (the major host for Zr, Hf) and garnet (the major host for HREE), there is unlikely to be any direct F and Cl effect. Therefore the variations of HREE and HFSE concentrations in melt reflect

the F and Cl effect on melt composition. As F and Cl represent major constituents in apatite, and we have observed an increase of LREE concentrations in apatite with the mole fraction of ClAp (see section 3.3 for details), the F and Cl effect on LREE in apatite must be taken into account when interpreting the variation of LREE contents in melt.

## 3 Results

### 3.1 Phase relations

All experimental runs produced a major mineral assemblage composed of garnet, phengite, quartz, and minor kyanite (Fig. 1a). Additionally, minor amounts of biotite were observed in some F-bearing experiments. Accessory phases, apatite, rutile and zircon were found in all experimental charges (Fig. 1). The presence of allanite was not apparent during the initial BSE imaging study, however trace amounts of allanite were detected as inclusions during LA-ICPMS analysis of quenched melt in the majority of the experiments. Note that the search for allanite using this method was not exhaustive. Normalized anhydrous melt compositions are granitic with near to constant $SiO_2$ contents (73.8 to 75 wt%), Si/Al (4.2-4.5) and Na+K/Al (0.70-0.84) molar ratios (Table A.1). The $H_2O$ content in melt is buffered by the residual mineral assemblage, and remains constant at fixed *PT* conditions, with an estimated value of 11-12 wt% based on mass balance calculations. Melt and mineral phase abundances (estimated from mass balance) are listed in Appendix Table A.3 for easy reference.

This set of experiments was designed to vary only bulk F and Cl contents, which results in the variation of F and Cl contents in melt and hydrous mineral phases. However, due to experimental variability, there was also a slight variation in melt fraction (48-62%), and a significant variation in the mass fraction of mica (5-15%). Cl and F contents in apatite vary in the ranges 0.33-2.67 wt% and 1.57-2.49 wt%, respectively; corresponding to molar fractions of ClAp and FAp in the ranges 0.048-0.401 and 0.42-0.67, respectively. By comparison, Cl and F contents in phengite (0.016-0.101 wt% Cl and 0.04-0.22 wt% F) and Biotite (0.10-0.23

wt% Cl and 0.30-0.60 wt% F) are significantly lower; thus the F and Cl effect on trace element concentrations in phengite and biotite was not investigated.

### 3.2 Variation of trace element compositions in melt

Melt trace element compositions are listed in Table 2, with normalized values (to the starting composition) plotted according to their incompatibility (Sun and McDonough, 1989) in Fig. 3. The melt composition of experiment C1846 from Hermann and Rubatto (2009), conducted at 2.5 GPa, 800°C with a Cl, F-free EPSM, is also plotted for comparison. All of the melt compositions show a consistent trace element pattern with enrichment of LILE, Pb, Th, U and LREE, positive Zr and Hf anomalies, and depleted HREE concentrations (Fig. 3). The most incompatible element observed in melt is Cs, with a normalized concentration $Cs_N$=2 ($Cs_N$=$Cs_{melt}$/$Cs_{EPSM}$).

In general, trace element concentrations in melt show up to 2 times variation between experiments (Table 2, Fig. 4-6). In order to separate the F effect from the effect of Cl, trace element concentrations are plotted against the Cl content in melt in three data groups based on the bulk Cl and F contents: “Cl”, “Cl+700ppmF” and “Cl+1500ppmF” (Fig. 4). As F in melt is proportional to the bulk F content, the melt compositions within each group have approximately the same F contents (Li and Hermann, 2017). The F effect can then be derived by comparing data points from the three different groups. As shown in Fig. 4, there is no discernible F effect on all but HFSE (Nb plotted as an example). Based on the different trends of variation with melt Cl/F content, or melt/mica mass fraction, eight groups of elements can be distinguished, with Cs, Ba, Fe, Ce, Dy, Ti, P and Nb plotted as examples. The concentrations of Li, Be, Sr and Cs are negatively correlated with the melt fraction (Fig. 4a). The concentrations of Rb and Ba show negative correlations with the mass fraction of mica (phengite+biotite) (Fig. 4b, A.1; Appendix A). The concentrations of Zn, V and Pb in melt are positively correlated with major elements Fe, Ca and Mg (Fig. A.2). An increase in concentration is observed for Zn, V, Pb, Fe, Ca and Mg with the increase of Cl content in

melt (Fig. 4c). The concentrations of light and medium rare earth elements (LMREE) also increase with the Cl content in melt (Fig. 4d, 5b). The concentrations of HREE and Y appear to first increase then decrease with increasing Cl content in melt (Fig. 4e, 5c). Sc and Mn show similar trends of variation as those observed for HREE (Fig. 5c). While the Ti content in melt stays constant, an increase in concentration is observed for P with increasing Cl content (Fig. 4f, g). Both Cl and F cause a decrease in the HFSE (Nb, Ta, Zr, Hf) concentrations in melt (Fig. 4h). Therefore, with the addition of F+Cl, the concentrations of HFSE show similar decreasing trends, with up to 2 times variation for Nb and Ta, and up to 20% variation for Zr and Hf (Fig. 6).

The melt composition of exp. C1846 has a LREE pattern (normalized to the starting compositions, Fig. 5a) which is mostly flat, followed by a decrease for medium rare earth elements (MREE), while the melt compositions of our experiments all have a steeper decreasing trend from La to Gd with a positive Eu anomaly. Such a difference suggests that, for our experiments, the melt concentrations of LMREE are controlled by the partitioning between apatite and melt, rather than the partitioning between allanite and melt, as is the case for exp. C1846. The steeper decreasing trend from LREE towards MREE can be explained by the affinity apatite has for MREE relative to LREE. This is commonly seen as a concave pattern in plots of apatite trace element compositions (e,g., Spandler et al., 2003) or apatite-melt partition coefficients (e.g., Watson and Green, 1981; Prowatke and Klemme, 2006). The effect of apatite composition on LMREE concentrations in melt can be demonstrated by the anomalous data point from exp. C3922 in Fig. 4d. Apatite from exp. C3922 has the highest mole fraction of ClAp and the highest Ce content (Table 3), which results in an abnormally low Ce concentration in melt. This can be understood from a simple mass balance point of view, or with the help of equation (2), i.e., higher Ce content in apatite means higher $D_{Ce}^{Ap\text{-}melt}$ and therefore lower Ce concentration in melt. As Cl has a positive effect on Ce content in apatite (see section 3.3 for details), which translates to a negative effect on Ce content in melt, the positive correlation between Ce and Cl in melt shown in Fig. 4d must be intrinsic.

With the exceptions of exp. C3922 and C3955, melt compositions have uniform $Th_N/U_N$ and $Th_N/La_N$ ratios, with average values of 0.6±0.1 and 1.6±0.2, respectively (Table 2). These are also similar to values for the allanite-buffered melt of exp. C1846 (Fig. 7a, b). As apatite contains more U than Th, and more La than Th (see section 3.3 for details), it is apparent that allanite is the dominant control for Th and U partitioning in all but two experiments (exp. C3922 and C3955). The higher $Th_N/U_N$ and $Th_N/La_N$ ratios for the melt of exp. C3955 suggest that apatite also plays an important role in the Th and U partitioning of exp. C3955, while the contribution of apatite is even greater, possibly dominant, for the Th and U partitioning of exp. C3922. In contrast, the $Sm_N/La_N$ for all experiments is distinctively lower than that for the melt of exp. C1846 (Fig. 7c), demonstrating the apatite control on LMREE partitioning. The role of apatite in terms of Th, U and LMREE partitioning will be discussed further in section 4.5.

The contrasting behaviors of LMREE, HREE and HFSE in response to varying Cl content in melt can be further demonstrated with elemental ratios, such as $Ce_N/Nb_N$, $Ce_N/Y_N$ and $Zr_N/Nb_N$. The $Ce_N/Nb_N$ ratio for melt displays a positive correlation with the Cl content in melt, with a 3 times increase over the investigated Cl range (Fig. 7d). The $Ce_N/Y_N$ ratio also increases with the Cl content in melt as shown in Fig. 7e; with the three anomalous data points below the trend inherited from the LREE and HREE variations (Fig. 4d, e). The $Zr_N/Nb_N$ ratio displays an increasing trend with the Cl content in melt, with values falling in the range 1.6 to 2.5 (Fig. 7f).

### 3.3 Variation of trace element compositions in apatite

The regression method used to derive trace element compositions for apatite proved effective, with the best correlations for LREE ($R^2$>0.98), less so for HREE ($R^2$=0.78-0.98), while for some experiments, Th and U were not constrained. Such a difference is mainly due to the fact that LREE are present in apatite at several thousand ppm, whereas the concentrations of HREE range from 100 to 300 ppm (Table 3), and Th and U in apatite were

only constrained with confidence for concentrations ~5 times higher than their contents in melt (12-40 ppm). Calculated with a mass fraction of 2%, apatite contains ~19% of the bulk Sr, > 80% of the bulk La, Ce, Pr and Nd, ~60% of the bulk Sm, ~40% of the bulk Eu and Gd, ~25% of the bulk Dy, <10% of the bulk Y, Er, Yb and Lu, ~13% of the bulk Th, and ~23% of the bulk U.

It appears that trace element concentrations in apatite are positively correlated with the mole fraction of chlorapatite ($X_{Cl}^{Ap}$) (Fig. 8). Such a variation is most prominent for Th and U (Fig. 8a), with a 4-5 times increase from $X_{Cl}^{Ap}$ = 0 (exp. C3927) to $X_{Cl}^{Ap}$ = 0.4 (exp. C3922). The positive correlation with $X_{Cl}^{Ap}$ is also apparent for Sr and LREE, but less so for HREE (Fig. 8b, c). When we calculate the relative increase of trace element concentrations in apatite from $X_{Cl}^{Ap}$ = 0 (exp. C3927) to $X_{Cl}^{Ap}$ = 0.4 (exp. C3922), a systematic pattern emerges (Fig. 8d). The degree of increase with $X_{Cl}^{Ap}$ is stronger for LREE than HREE, appearing to be positively correlated with ionic radii. Similar trends may also exist for 4+ and 2+ cations, respectively. It is also apparent that the relative increase in concentration with $X_{Cl}^{Ap}$ is higher for cations with higher charge, e.g., $Th^{4+}$, $U^{4+}$ > $REE^{3+}$. In contrast to the uniformity observed in the ratios of $Th_N/U_N$, $Th_N/La_N$ and $Sm_N/La_N$ for melt, these ratios for apatite show pronounced variations (Fig. 9), which reflect the relative sensitivity of these elements to the increase of $X_{Cl}^{Ap}$, i.e., Th>U, Th>La and Sm<La.

### 3.4 Trace element partitioning between apatite and melt

The LMREE partition coefficients between apatite and melt ($D_{LMREE}^{Ap\text{-}melt}$) show a concave pattern with the highest value for Sm/Nd and a negative Eu anomaly (Fig. 10). For experiments C3269, C3922 and D1218, the HREE partition coefficients ($D_{HREE}^{Ap\text{-}melt}$) are well constrained and extend the concave pattern shown by LMREE partition coefficients. For all other experiments $D_{HREE}^{Ap\text{-}melt}$ values have higher uncertainties, which may have contributed to the dubious nature of their flat trend (Fig. 10). Partition coefficients for LMREE show up to 4 times variation between experiments, e.g., $D_{La}^{Ap\text{-}melt}$ = 77-281 and $D_{Sm}^{Ap\text{-}melt}$ = 176-519

(Table 4). Partition coefficients for Sr vary from 4 to 12. The values for Th and U partition coefficients are slightly higher, falling in the range 4-19 (Table 4). The variations of trace element partition coefficients between apatite and melt reflect both the variation of melt composition with Cl (Fig. 11a) and the variation of apatite composition with $X_{Cl}^{Ap}$ (Fig. 11b, c).

Partition coefficients for REE (excluding Eu) and Y were fitted to the lattice strain model of Blundy and Wood (1994):

$$D_i = D_0 \exp\left[\frac{-4\pi N_A E\left[\frac{r_0}{2}\left(r_i - r_0\right)^2 + \frac{1}{3}\left(r_i - r_0\right)^3\right]}{RT}\right] \quad (4)$$

where $N_A$ is the Avogadro constant, $R$ is the gas constant, $T$ is in Kelvins, $E$ is the Young's modulus of the site, $r_0$ is the optimum radius of the lattice site, $r_i$ is the radius of the substitute cation, and $D_0$ describes the strain-free cation substitution ($r_i = r_0$). REE can substitute into both Ca1 ($Ca1O_9$ polyhedra) and Ca2 ($Ca2O_6X$, X=F, Cl, OH) sites in apatite. The review by Pan and Fleet (2002) summarized that LREE prefer the Ca2 site of FAp and OHAp with the site occupancy ratio (REE-Ca2/REE-Ca1) decreasing monotonically through the 4*f* series. Fleet et al. (2000) reported that REE in ClAp preferentially occupy the Ca1 site with the exception of Nd, which has a marginal preference for the Ca2 site. Considering the foreseeable complexity of REE site occupancy in F-Cl-OH ternary apatite solutions, fitting with the lattice strain model was performed with both VII and IX coordinated ionic radii for REE respectively. For each experiment, separate regressions were performed with partition coefficients for [1]LREE (La-Sm/Gd), HREE (Sm/Gd-Lu) and all REE, respectively. The fitting with HREE data was not as successful as that for LREE, with parameters returned for only exp. D1218. This is not surprising considering the large relative errors for HREE partition

[1] In regards to fitting of the lattice strain model, "LREE" and "HREE" refer to the data used for regression; where "LREE" represents LREE±MREE (Sm, Gd).

coefficients, and thus those involving particularly large uncertainties were omitted in the fitting of all REE data, in order to obtain meaningful parameters.

Fitting with IX coordinated ionic radii gave slightly lower values for Young's modulus ($E$) compared to fitting with VII coordinated ionic radii, but in general, the results were very similar. The obtained $E$ values from fitting LREE data fall within the range 134-256 GPa, while fitting all REE returned $E$ values in the range 140-411 GPa (Table 5). As shown by the fitting of partition coefficients for exp. D1218 (Fig. 12a, b), the regressed $E$ value from fitting LREE is lower than that from fitting HREE data. The $E$ value from fitting all REE is likely to be the weighted mean of the values from fitting LREE and HREE data (Fig. 12c). A gentle increase with $X_{Cl}^{Ap}$ can be seen for $E$ values derived from fitting LREE data. Judging from the relationship between $E$ values from fitting all REE and $X_{Cl}^{Ap}$, a similar trend may well exist for $E$ values from fitting HREE (Fig. 12c). One of the presumptions of the lattice strain model is that the elements in question have identical activity coefficients in melt (Wood and Blundy, 2014). This may hold true for LREE and HREE respectively, but activity coefficients may vary between the two groups. For example, LREE and HREE show different behavior with the Cl content in melt. Nevertheless, fitting with all REE data proved to be informative, as it provided a good indication of the range of $E$ values from fitting HREE. Considering the limited success in fitting HREE, the parameters from fitting all REE will be particularly useful when predicting HREE partition coefficients based on the lattice strain model.

## 4 Discussion

### 4.1 Comparison with reported solubility data

The concentrations of P, Ti and Zr in melt are buffered by the accessory phases apatite, rutile and zircon, respectively, i.e., the concentrations of these elements represent the solubility of the corresponding accessory phase. The range of P concentrations in melt (718-1064 ppm) is comparable to the apatite solubility (0.04-0.28 wt%) for felsic magma at 0.1 GPa, 750-900°C reported by Watson and Capobianco (1981). Ti contents in melt (732-866

ppm) are comparable to previously reported values for rutile-buffered melt at 2.5 GPa, 800°C, e.g., 948±18 ppm for exp. C1846 from Hermann and Rubatto (2009); and 882±270 ppm for exp. 16 from Klimm et al. (2008). The rutile solubility equation from Hayden and Watson (2007) also predicts ~1000 ppm Ti for felsic melt in equilibrium with rutile at 800°C. Zr contents in melt (71-89 ppm) are comparable to the reported values for exp. C1846 of Hermann and Rubatto (2009) (75±2.1 ppm) and exp. 16 of Klimm et al. (2008) (76±7 ppm). Zr contents in melt are also similar to reported values for zircon-buffered granitic melts in studies conducted under differing pressure conditions, for example, 82±2 and 92±1 ppm for the two experiments at 2 GPa, 800°C (exp. 1743 and exp. 1587A) from Rubatto and Hermann (2007); and 81±6 ppm for exp. LCA2B of 3 GPa, 800°C from Carter et al. (2015).

Keppler (1993) reported an increase in Ti, Zr, Nb and Ta solubility in haplogranitic melt with the addition of F at 0.2 GPa and 800°C. For example, the $TiO_2$ content in melt increased from 0.26 wt% at zero F to 0.47 wt% at 6 wt% F. The positive effect of F on HFSE solubility can be explained by an increase in depolymerization of melt structure over the F compositional range 0-6 wt%. However, for the low F concentrations investigated in this study, such an effect on HFSE is difficult to detect. Keppler (1993) also observed ~2 times variation for REE phosphate solubility over the 0-6 wt% F range, however with limited data points available, no clear positive or negative effect was determined. It is interesting to note that Keppler (1993) also observed an initial increase followed by a decrease in Yb concentration with increasing F content in melt.

### 4.2 Understanding the F and Cl effect on trace element concentrations in melt

The effect of F and Cl on trace element concentrations in melt arises from the depolymerization induced by F and Cl on melt structure and the complexing of F and Cl with trace elements. NMR spectroscopic studies have indicated that F forms complexes with Al, Na, and Si in aluminosilicate glasses (Kohn et al., 1991; Mysen et al., 2004; Schaller et al., 1992; Zeng and Stebbins, 2000). Cl coordination with network-modifying cations has been

suggested by studies using NMR (Sandland et al., 2004), IR (Chevychelov et al., 2003) and XANES (Evans et al., 2008). However, limited information is available regarding the complexation of F and Cl with trace elements in silicate melt. Pioneering XAS studies of REE and HFSE in silicate melt and glass at ambient conditions indicate that Zr (Farges et al., 1991), Th (Farges, 1991) and U (Farges et al., 1992) do not form complexes with F or Cl, but coordinate with oxygens from $SiO_2$ tetrahedra. Ponader and Brown (1989a) found no evidence for REE-Cl complexes, whereas, F complexing with La, Gd and Yb was indicated. These studies also reported variations in coordination from 6-8 fold for Gd, La (Ponader and Brown, 1989b), Zr (Farges et al., 1991), Th (Farges, 1991) and U (Farges et al., 1992); 5-6 fold for Yb (Ponader and Brown, 1989b); and 4-6 fold for Ti (Farges and Brown, 1997), in response to changes in the degree of melt polymerization within the compositional range of basaltic (NBO/T≈1) to rhyolitic (NBO/T≈0) melts. The F and Cl melt contents in this study (650-3000 ppm) are unlikely to induce the variation of melt polymerization required to change the coordination of trace elements in melt. Moreover, recent high pressure and temperature XAS studies reported uniform 6-fold coordination for Zr (Louvel et al., 2013), Nb (Mayanovic et al., 2007; Piilonen et al., 2006) and Ta (Mayanovic et al., 2013) in hydrous silicate melts, apparently independent of melt composition.

The positive correlations between the concentrations of trace elements Zn, V, Pb and major network-modifiers Fe, Ca and Mg in melt, suggest that the increase in concentration for Zn, V and Pb with the Cl content may be explained by their complexation with Cl. Note that there may be a small percentage of Fe present as $Fe^{3+}$ (see section 2.2), however, as proposed by Mysen and Virgo (1985), $Fe^{3+}$ may undergo a coordination transformation from tetrahedral to octahedral and become a network modifier at high pressure. Therefore we are not distinguishing $Fe^{2+}$ and $Fe^{3+}$ in our current discussion. Increasing network-modifier contents in melt will result in an increase of non-bridging oxygens (NBO), which will further facilitate the accommodation of network-modifying cations. The positive Cl effect on REE contents may be an indirect result of the complexation of Cl with network-modifiers (e.g., Fe, Mg, Ca,

Zn, V and Pb). As most geochemically significant trace elements are network-modifiers, the depolymerization effect of F and Cl on melt structure would cause an increase of trace element concentrations in general. However, HFSE show a decrease in concentration with the F+Cl content in melt. We therefore further explore the relationships between trace element concentrations in melt and melt structure through $Q^n$ speciation theory.

Melt structure can be described by the speciation of silicate or aluminosilicate tetrahedra, i.e., $Q^n$ species, where n is the number of bridging oxygens in the tetrahedra. Five $Q^n$ species, $Q^4$, $Q^3$, $Q^2$, $Q^1$, $Q^0$, may be present in melt (Stebbins, 1987). Their relative proportions are functions of the degree of melt polymerization, field strength of network-modifying cations, Al/Al+Si (see the review by Mysen, 2004) and volatile ($H_2O$, F and Cl, etc.) contents (Dalou and Mysen, 2015; Mysen, 2007). For the hydrous granitic melt compositions in this study, the dominant $Q^n$ species are $Q^4$ and $Q^3$ with a small fraction of $Q^2$ as a result of the high $H_2O$ content (~11 wt%). The Raman spectroscopic study of hydrous aluminosilicate melts at 1.5 GPa, 1400°C by Dalou and Mysen (2015) indicated an increase of $Q^3$ and $Q^1$ species, and a decrease of $Q^2$ and $Q^4$ species with the addition of F and Cl in melt. It is known that non-bridging oxygens of different $Q^n$ species in melt are energetically non-equivalent, and cations will likely form bonds with their preferred $Q^n$ species (Mysen, 2004). It is therefore likely that, with the addition of F and Cl in melt, trace elements with raised concentrations (LMREE, Th, U) form bonds with $Q^3$, whereas, HFSE (Nb, Ta, Zr, Hf) with lowered concentrations coordinate with $Q^2$. This is consistent with the current understanding that cations with higher field strength, form bonds with more depolymerized $Q^n$ species (Stebbins, 2016). The behavior of HREE may be intermediate between LMREE and HFSE, due to their intermediate cation field strengths. Therefore, the initial increase followed by a decrease in HREE concentrations may be a result of HREE coordinating with both $Q^2$ and $Q^3$ species. A study of P-bearing silicate glass by multinuclear NMR and ab initio chemical shielding calculations (Cody et al., 2001) indicated complex P speciation in silicate glasses, including isolated $PO_4$ and $P_2O_7$ complexes, and $Q_P^n$ (n=1-4) species. The solution mechanisms

proposed for P involve the interaction of $P_2O_5$ with $Q_{Si}^3$ species and the formation of $Q_{Si}^4$ species (Mysen and Cody, 2001). Therefore, enhanced P solubility in melt may be explained by an increasing proportion of $Q_{Si}^3$ and a decreasing proportion of $Q_{Si}^4$ with the increase of Cl content in melt. It is noteworthy that only a negative correlation between HFSE and F contents in melt was observed, while no discernible F effect was shown for other trace elements. This may indicate that Cl has a more pronounced effect on trace element uptake in melt at a similar magnitude of concentration.

### 4.3 Comparison with Ap-melt partitioning data from previous studies

Trace element partition coefficients between apatite and melt obtained in this study have higher values than those reported in previous experimental studies (Fig. 10). Detailed comparisons are listed below using Sm as an example. Watson and Green (1981) determined REE partition coefficients (La, Sm, Dy, Lu) between FAp/OHAp and melts ranging from basanite to granite at *PT* conditions of 0.75-2 GPa, 950-1120°C. The resultant $D_{Sm}^{\text{Ap-melt}}$ values range from 4.5 to 38, increasing with the $SiO_2$ content in melt and decreasing with temperature, with the highest value 38 corresponding to Sm partitioning between F-OH apatite and a hydrous granitic melt at 0.75 GPa, 950°C. Prowatke and Klemme (2006) reported trace element partition coefficients between FAp/OHAp and $H_2O$/F-bearing silicate melts at 1 GPa, 1250°C, with $D_{Sm}^{\text{Ap-melt}}$ varying in the range 3.7-28 in response to changes in the degree of melt polymerization. Fleet and Pan (1997) determined $D_{Sm}^{\text{Ap-melt}}$ between FAp and $H_2O$-bearing phosphate-fluoride melts at 0.10-0.15 GPa, 700 and 800°C, with values in the range 3.5-8.8. REE partition coefficients between ClAp and phosphate-chloride melt are much lower, with reported values of 0.12 for $D_{Sm}^{\text{Ap-melt}}$ at 0.1 GPa, 735°C by Fleet et al. (2000). REE partition coefficients for carbonatite melt are of the same magnitude as those for phosphate-chloride melt, with reported $D_{Sm}^{\text{Ap-melt}}$ values of 0.43-0.55 at 1 GPa, 1250°C (Klemme and Dalpé, 2003). It is apparent that melt composition and *PT* conditions are the primary controls on *D* values. In comparison to the partition coefficients reported previously,

the higher values obtained in this study ($D_{Sm}^{\text{Ap-melt}}$=176-519) seem reasonable considering the low temperature (800°C) and high pressure (2.5 GPa) experimental conditions, and the granitic melt composition.

It is important to isolate both the crystal-chemical control and the melt compositional effect when comparing the partition coefficients for ClAp, FAp and OHAp. Despite the prediction of LREE enrichment in ClAp by Fleet and Pan (1997), the LREE partition coefficients between ClAp and phosphate-chloride melt are much lower than the partition coefficients between FAp and phosphate-fluoride melt (Fig. 10), suggesting greater melt compositional control. Klemme and Dalpé (2003) did report REE partition coefficients between ClAp and carbonatite melt as being slightly larger than those for FAp and OHAp. The REE partition coefficients for F-bearing experiments reported in Prowatke and Klemme (2006) are 2-3 times higher than those for $H_2O$-bearing experiments (compare exp. 43 vs 72; exp. 54 vs 78, respectively). However, the difference in partition coefficients for Sr is <1.5×, and negligible for Th and U. As shown by the correlations between apatite trace element concentrations and the mole fraction of ClAp, trace element uptake in apatite strongly depends on cation size and charge (Fig. 8). Based on the observation that the increase of REE partition coefficients for F-bearing experiments compared to $H_2O$-bearing experiments is nearly uniform, and the consideration that FAp and OHAp have similar molar volumes, we suspect that apatite composition may not be a significant contributing factor to the difference in partition coefficients. Higher REE partition coefficients for the F-bearing experiments of Prowatke and Klemme (2006) may be explained solely by the lesser degree of depolymerization for melt compositions with 2-3 wt% F in comparison to melt compositions with 5 wt% $H_2O$.

To our knowledge, this study is the first to provide strong experimental evidence supporting the prediction of Fleet and Pan (1997) that ClAp favors the accommodation of LREE. The rarity of such observations in experimental literature can be attributed to the following factors. Firstly, there have been limited experimental studies on trace element

partitioning involving ClAp or Cl-bearing apatite. Secondly, as we have shown in this study, Cl has a positive effect on LREE contents in both melt and apatite. Such effects may cancel out and become difficult to detect in reported partition coefficients between apatite and melt. Thirdly, the melt compositional effect may dominate when the melt compositions are drastically different, e.g., phosphate-fluoride melt vs. phosphate-chloride melt. For the experiments of this study, REE partition coefficients between apatite and melt have such high values that their variations are easy to detect. Moreover, we were able to isolate both the crystal-chemical control and the melt compositional effect on the partition coefficients. As demonstrated by the $Th_N/U_N$, $Th_N/La_N$ and $Sm_N/La_N$ ratios for melt in Fig. 7 and for apatite in Fig. 9, LMREE, Th and U display nearly uniform variations with the Cl content in melt; while the effect of $X_{Cl}^{Ap}$ on trace element concentrations in apatite depends on cation size and charge.

### 4.4 Fitting $D_{REE}^{Ap\text{-}melt}$ with the lattice strain model

The parabola of $D_{REE}^{Ap\text{-}melt}$ vs. ionic radii was successfully fitted with the lattice strain model of Blundy and Wood (1994). This signifies that size and elasticity of the apatite structure has a fundamental control on the REE uptake in apatite. Regardless of the complexity of REE site occupancy in apatite, Nd/Sm represents the strain free substitution for Ca. The increasing LREE contents in apatite with $X_{Cl}^{Ap}$ can be explained by an increase in size for Ca2 polyhedra with the substitution of Cl for F/OH, which facilities the accommodation of large LREE cations. Such enrichment of LREE in ClAp was predicted by Fleet and Pan (1997), based on ideal bond distance calculations. Both the bulk modulus and Young's modulus are positively correlated with cation charge (Wood and Blundy, 2014); which may be understood as cations with higher charges are stiffer and more constrained by the size of the lattice site. This may explain our observation that the relative increase in concentration with $X_{Cl}^{Ap}$ is higher for 4+ cations (Th, U) than for $REE^{3+}$.

The REE partition coefficients between apatite and melt reported in previous experimental studies all show a concave pattern (Fig. 10). They were also fitted to the lattice strain model of Blundy and Wood (1994), following the same procedures used in this study, with the fitting parameters listed in Table 6. Regressed *E* values lie in the range 100-300 GPa, similar to the range of values obtained in this study. These *E* values are comparable to the bulk modulus for apatite, which has been determined to be between 90-100 GPa (Brunet et al., 1999; Comodi et al., 2001; Matsukage et al., 2004). In particular, Comodi et al. (2001) reported bulk modulus values of 270±10, 100±4, and 86±3 GPa for P, Ca1 and Ca2, respectively. It seems that the bulk modulus of apatite is similar to that of Ca polyhedra, with the bulk modulus for Ca1 higher than that for Ca2. This explains our observation that the *E* values derived from fitting HREE data are higher than the *E* values from fitting LREE, considering the relative preference for HREE to substitute for Ca1 and for LREE to substitute for Ca2.

Fitting with IX coordinated ionic radii gave slightly smaller *E* values than fitting with VII coordinated ionic radii, but in general the results were very similar (Table 6). The *E* values derived for experiments from Klemme and Dalpé (2003) are smaller and better constrained than their reported values, which were derived using VI coordinated ionic radii. Few *E* values were derived from fitting LREE or HREE data. Only exp. BS19 of Klemme and Dalpé (2003) and the experiment of Fleet et al. (2000) were performed with ClAp, with all other experiments conducted with F-OH apatite. Due to this lack of data, we were unable to derive a clear relationship between *E* values and the mole fraction of ClAp, or observe differences between *E* values derived from fitting LREE and HREE data respectively.

### 4.5 The role of apatite in trace element recycling in subduction zones

In this study, apatite-melt partitioning provides the dominant control on the LMREE concentrations in melt. The positive Eu anomaly seen in the REE diagram for melt (Fig. 5a) can be explained by the lower apatite-melt partition coefficient for Eu compared to Sm and

Gd (Fig. 10), which is likely due to Eu occurring in both 2+ and 3+ valence states. Moreover, when apatite is the dominant host of the LMREE budget, the coexisting melt has a different LMREE pattern than that of a melt buffered by allanite/monazite (Fig. 5a), e.g., lower $Sm_N/La_N$ (Fig. 7c).

Apatite contains >80% of the bulk LREE, but only ~13% of the bulk Th. The low $Th_N/La_N$ ratios in apatite (0.07-0.18, Table 3) indicate its ability to significantly fractionate Th from La in melt. Moreover, apatite has a preference for U over Th, with $Th_N/U_N$ values of 0.5-0.7 (Table 3); therefore an apatite-buffered melt will have Th enrichment relative to U. This is in clear contrast to the role of residual allanite and monazite, which were reported to incorporate Th in preference to U.

The melt compositions of exp. C3922 and C3955 have higher $Th_N/U_N$ and $Th_N/La_N$ ratios in comparison to the uniform $Th_N/U_N$ (0.6±0.1) and $Th_N/La_N$ (1.6±0.2) ratios for all other experiments (Table 2, Fig 7a, b). Such a difference suggests that apatite also plays an important role in the Th and U partitioning of exp. C3922 and C3955. Such an interpretation is further supported by the La, Ce and Th mass balance (Table 3), where apatite contents were calculated, assuming melt and apatite take up the entire La, Ce and Th budget. The calculated La and Ce concentrations in apatite for exp. C3922 and C3955 are the closest to the regressed values, indicating that these elements are primarily hosted by melt and apatite. For all other experiments, calculated concentrations in apatite (Th in particular) are far higher than the regressed values from LA-ICPMS analysis. The differences in these values represent the portion of La, Ce and Th accommodated by allanite. It is apparent that even when apatite accommodates >80% of the LREE budget, allanite is still the main host for Th. Allanite-melt partition coefficients for Ce at 2.5 GPa, 800°C are determined to be ~2000 by Klimm et al. (2008), adopting this value will result in an estimate of 4-8 wt% Ce in allanite. Based on Ce mass balance, the mass fraction for allanite is estimated to vary in the range ~0.01% (e.g., exp. C3955) to ~0.1% (e.g., exp. D1222). For such small amounts of allanite, it is not surprising that they are difficult to detect. The low allanite fraction in exp. C3955 and C3922, i.e.,

greater contributions from apatite in terms of Th and U partitioning, provides an explanation for their higher $Th_N/U_N$ and $Th_N/La_N$ ratios in melt.

It has been shown that there is no significant fractionation between Th and La during sediment melting in most subduction zones, indicating the dominance of monazite in terms of LREE and Th partitioning (Plank, 2005). However, apatite-allanite partitioning may play an important role during partial melting of high-Ca sediment (Plank, 2005) and oceanic crust (Carter et al., 2015; Klimm et al., 2008). The ratio between the Th/La of Tonga arc basalt and the Th/La of sediment (Plank, 2005), is identical to the $Th_N/La_N$ value (1.6±0.2) for allanite or apatite+allanite buffered melt compositions. To explain the higher ratio of 2.4 between Guatemala arc basalt and sediment (Plank, 2005), requires a greater contribution from apatite partitioning, as in the case of exp. C3955 with $Th_N/La_N$=2.7. Apatite may also facilitate further fractionation between Th and La during arc crust differentiation, resulting in an elevated Th/La ratio for the bulk continental crust (Plank, 2005).

Our study has shown that the capacity of apatite to host trace elements increases with an increasing mole fraction of ClAp (Fig. 8). Reports on the Cl contents in subduction-related apatite are scarce. Our previous study reported Cl contents of ~100 ppm for apatites from eclogite facies matasediments (Li and Hermann, 2015). Apatite compositions with significant Cl contents were obtained from UHP metamorphic rocks of the Kokchetav (up to 0.6 wt%) and Dora Maira massifs (up to 2.5 wt%) (Li, 2012). To assess the significance of Cl-bearing apatite on trace element recycling requires an inventory of halogen contents in subduction-related apatites and further experimental studies. Current understanding of the capacity of saline aqueous fluids to transport LILE, LREE and U are based on partitioning experiments between clinopyroxene and aqueous fluids (Brenan et al., 1995; Keppler, 1996), and solubility studies of monazite (Tropper et al., 2011) and $REE_2Si_2O_7$ (Tsay et al., 2014). Unlike apatite, these minerals do not change their capacity for trace element incorporation with addition of Cl. As apatite is a common accessory phase in all rock types present in subducted crust, it would be wise to include apatite in future aqueous fluid partitioning experiments.

### 4.6 The role of F and Cl in trace element recycling in subduction zones

While residual mineral phases provide the dominant control on trace element characteristics in sediment melt (Hermann and Rubatto, 2009; Hermann, 2002; Klimm et al., 2008; Skora and Blundy, 2010), we have shown in this study that F and Cl can also contribute to fractionation between LREE and HREE, fractionation between LREE and HFSE, and fractionation between Zr and Nb (Fig. 7). Rutile is the main host for Nb and Ta whereas zircon is the main host for Zr and Hf. As the Ti and Zr contents in EPSM are similar to the average values for GLOSS, the $Nb_N$, $Ta_N$, $Zr_N$ and $Hf_N$ values are applicable to the GLOSS composition. The $P_2O_5$ content in EPSM is around 5 times that of GLOSS (Table 1), i.e., the mass fraction of apatite for a GLOSS composition will be only 1/5 of the value for EPSM. Such a significant decrease in the amount of residual apatite will result in a 2-4 times increase for the normalized LREE values. For example, the $Ce_N/Nb_N$ ratios in melt have a range of values 1.7-3.7 after correction for apatite mass fraction, with higher values corresponding to the higher F+Cl content in melt. We recalculated the normalized Th, La, Ce, Pr, Nd and Sm concentrations in melt for exp. C3922 with a corrected apatite mass fraction for the GLOSS composition, using equation (3) and apatite-melt partition coefficients determined for exp. C3922. As shown by the comparison in Fig. 3, the $Zr_N$ and $Hf_N$ positive anomaly, relative to $Sm_N$ and $Nd_N$, becomes far less prominent. As the REE contents in experimental starting compositions are always higher than those of GLOSS, similar corrections to the normalized LREE contents in melt apply to other experimental studies involving allanite and monazite as the main mineral hosts for LREE. As the Cl content in melt increases, $Zr_N/Nb_N$ for melt varies in the range 1.6-2.5, higher than the $Zr_N/Nb_N$ value of 0.8 for the F, Cl-free exp. C1846 (Fig. 7f). With a Zr/Nb ratio of 14.5 in GLOSS, sediment melt produced by ~50% melting of GLOSS at 2.5 GPa, 800°C will have a Zr/Nb ratio in the range of 23 to 36, which is comparable to the reported values for both MORB and arc magmas (e.g., Elliott et al., 1997). When modelling the partial melting of subarc mantle with the addition of a subduction

component, HFSE (Nb, Ta, Zr, Hf) in arc magmas have been assumed to be entirely derived from the mantle wedge (e.g. Portnyagin et al., 2007). However, if the subduction component (e.g., sediment melt) contributed to the mass balance of Zr/Nb in arc magmas, it is plausible to suggest Cl could be responsible for the fractionation of Zr and Nb.

It is interesting to note that the Cl effect on element fractionation in sediment melt is similar to the reported enhancement of element fractionation with the addition of Cl in aqueous fluids (Brenan et al., 1995; Keppler, 1996; Tsay et al., 2014), which has been used as supporting evidence for Cl-bearing aqueous fluids as the medium for trace element recycling. The most recent argument put forward by Keppler (2017) is based on the positive correlations between element/$H_2O$ and Cl/$H_2O$ ratios for melt inclusions from Mexico and Kamchatka arc basalts. We have shown in this study that such an observation could arise from the positive correlations between trace element contents and the Cl in melt. The arguments supporting aqueous fluids as the dominant medium for transporting incompatible elements rely heavily on the enhancement of LREE solubility in saline aqueous fluids. Tropper et al. (2011) reported that $CePO_4$ monazite dissolution into an $H_2O$-NaCl fluid with $X_{NaCl}$~0.1 (~26 wt% NaCleq) at 1 GPa, 800°C, can produce a Ce concentration of 140 ppm and $H_2O$/Ce of 7000, identical to the ratio for slab melt at 800°C (Plank et al., 2009). This indicates that for aqueous fluid to achieve melt-like solubility and $H_2O$/LREE ratios, it requires very high levels of salinity (e.g., ~26 wt% NaCleq, Tropper et al., 2011). Aqueous fluids formed during subducted slab dehydration have been shown to have low salinity, in many cases, below the salinity of seawater (~3.2% NaCleq) (Li and Hermann, 2015). For example, Tsay et al. (2017) reported the La contents in $H_2O$ and 1m NaCl fluid (~5.5 wt% NaCleq) at 2.5 GPa, 700°C, in equilibrium with allanite-bearing eclogite mineral assemblages, to be 1.53±0.7 ppm and 0.84±0.44 ppm, respectively. The resulting $H_2O$/LREE ratios are far too high to be consistent with the $H_2O$/LREE ratios of arc lavas.

Our experiments help to evaluate the extent to which the addition of Cl in hydrous granitic melts affects the usage of the $H_2O$/Ce ratio as a slab geothermometer. The Ce content in melt

increased by a factor of <2 over the $H_2O$/Cl range 25-100 (1.6-6.4 wt% NaCleq) investigated in this study, which is typical for arc magmas. As for the proposed slab geothermometer, the $H_2O$/Ce ratio varies from $10^6$ to $10^2$ over the temperature range 600°C-1100°C (Plank et al., 2009). Therefore, variations in the $H_2O$/Ce ratio in response to changes in the nature of the fluid phase (aqueous fluid, intermediate supercritical fluid, hydrous melt) and temperature, are greater than the effect of Cl addition in melt.

## 5 Conclusions

By comparing trace element compositions of melt from a set of experiments using an EPSM starting composition with variable bulk F and Cl contents, we were able to observe the effect of F and Cl on trace element uptake in sediment melt, notably an enrichment of LREE relative to HFSE. Such an effect is similar to the fractionation observed for saline aqueous fluids. We also observed positive correlations between trace element concentrations (LMREE, Sr, Th, U) in apatite and the mole fraction of ClAp, therefore providing the first experimental evidence to support the prediction that ClAp favors the accommodation of LREE. Because LMREE, Th and U display uniform variations with the Cl content in melt, while the effect of $X_{Cl}^{Ap}$ on trace element concentrations in apatite depends on cation size and charge, we were able to isolate both the melt compositional effect and the crystal-chemical control on trace element partitioning. Considering such high values of $D_{LREE}^{Ap\text{-}melt}$ (e.g., $D_{La}^{Ap\text{-}melt}$ = 77-281, $D_{Sm}^{Ap\text{-}melt}$ = 176-519), the inclusion of apatite in models used to evaluate subduction recycling of incompatible trace elements is recommended.

## Acknowledgement

We would like to thank D. Clark and D. Scott for their assistance with the experimental program, and F. Brink and R. Rapp for their help with SEM and electron microprobe analyses. Comments and suggestions from James Brenan and an anonymous reviewer have helped us greatly to improve the manuscript. The editorial handling by Catherine Chauvel is

sincerely appreciated. This project was supported financially by the Australian Research Council.

**References**

Antignano, A., Manning, C.E., 2008. Fluorapatite solubility in H2O and H2O–NaCl at 700 to 900 °C and 0.7 to 2.0 GPa. Chem. Geol. 251, 112–119. doi:10.1016/j.chemgeo.2008.03.001

Auzanneau, E., Vielzeuf, D., Schmidt, M.W., 2006. Experimental evidence of decompression melting during exhumation of subducted continental crust. Contrib. to Mineral. Petrol. 152, 125–148. doi:10.1007/s00410-006-0104-5

Bali, E., Audétat, A., Keppler, H., 2011. The mobility of U and Th in subduction zone fluids: an indicator of oxygen fugacity and fluid salinity. Contrib. to Mineral. Petrol. 161, 597–613. doi:10.1007/s00410-010-0552-9

Bali, E., Keppler, H., Audetat, A., 2012. The mobility of W and Mo in subduction zone fluids and the Mo–W–Th–U systematics of island arc magmas. Earth Planet. Sci. Lett. 351-352, 195–207. doi:10.1016/j.epsl.2012.07.032

Bernini, D., Audétat, A., Dolejš, D., Keppler, H., 2013. Zircon solubility in aqueous fluids at high temperatures and pressures. Geochim. Cosmochim. Acta 119, 178–187. doi:10.1016/j.gca.2013.05.018

Blundy, J., Wood, B., 1994. Prediction of crystal-melt partition coefficients from elastic moduli. Nature 372, 452–454. doi:10.1038/372452a0

Brenan, J.M., Shaw, H.F., Ryerson, F.J., Phinney, D.L., 1995. Mineral-aqueous fluid partitioning of trace elements at 900°C and 2.0 GPa: Constraints on the trace element chemistry of mantle and deep crustal fluids. Geochim. Cosmochim. Acta 59, 3331–3350. doi:10.1016/0016-7037(95)00215-L

Brunet, F., Allan, D.., Redfern, S.A.T., Angel, R.J., Miletich, R., Reichmann, H.J., Sergent, J., Hanfland, M., 1999. Compressibility and thermal expansivity of synthetic apatites,

Ca5(PO4)3X with X = OH, F and Cl. Eur. J. Mineral. 11, 1023–1036. doi:10.1127/ejm/11/6/1023

Carter, L.B., Skora, S., Blundy, J.D., De Hoog, J.C.M., Elliott, T., 2015. An Experimental Study of Trace Element Fluxes from Subducted Oceanic Crust. J. Petrol. 56, 1585–1606. doi:10.1093/petrology/egv046

Chevychelov, V.Y., Simakin, A.G., Bondarenko, G. V, 2003. Mechanism of chlorine dissolution in water-saturated model granodiorite melt: Applications of IR spectroscopic methods. Geochemistry Int. 41, 395–409.

Cody, G.D., Mysen, B.O., Sághi-Szabó, G., Tossell, J.A., 2001. Silicate-phosphate interactions in silicate glasses and melts: I. A multinuclear (27Al,29Si,31P) MAS NMR and ab initio chemical shielding (31P) study of phosphorous speciation in silicate glasses. Geochim. Cosmochim. Acta 65, 2395–2411. doi:10.1016/S0016-7037(01)00597-X

Comodi, P., Liu, Y., Zanazzi, P.F., Montagnoli, M., 2001. Structural and vibrational behaviour of fluorapatite with pressure. Part I: in situ single-crystal X-ray diffraction investigation. Phys. Chem. Miner. 28, 219–224. doi:10.1007/s002690100154

Dalou, C., Mysen, B.O., 2015. The effect of H2O on F and Cl solubility and solution mechanisms of in aluminosilicate melts at high pressure and high temperature. Am. Mineral. 100, 633–643. doi:10.2138/am-2015-4814

Eggins, S.M., Kinsley, L.P.J., Shelley, J.M.G., 1998. Deposition and element fractionation processes during atmospheric pressure laser sampling for analysis by ICP-MS. Appl. Surf. Sci. 127-129, 278–286. doi:10.1016/S0169-4332(97)00643-0

Elliott, T., Plank, T., Zindler, A., White, W., Bourdon, B., 1997. Element transport from slab to volcanic front at the Mariana arc. J. Geophys. Res. Solid Earth 102, 14991–15019. doi:10.1029/97JB00788

Evans, K.A., Mavrogenes, J.A., O'Neill, H.S., Keller, N.S., Jang, L.-Y., 2008. A preliminary investigation of chlorine XANES in silicate glasses. Geochemistry, Geophys.

Geosystems 9, n/a–n/a. doi:10.1029/2008GC002157

Farges, F., 1991. Structural environment around Th4+ in silicate glasses: Implications for the geochemistry of incompatible Me4+ elements. Geochim. Cosmochim. Acta 55, 3303–3319. doi:10.1016/0016-7037(91)90490-V

Farges, F., Brown, G.E., 1997. Coordination chemistry of titanium (IV) in silicate glasses and melts: IV. XANES studies of synthetic and natural volcanic glasses and tektites at ambient temperature and pressure. Geochim. Cosmochim. Acta 61, 1863–1870. doi:10.1016/S0016-7037(97)00050-1

Farges, F., Ponader, C.W., Brown, G.E., 1991. Structural environments of incompatible elements in silicate glass/melt systems: I. Zirconium at trace levels. Geochim. Cosmochim. Acta 55, 1563–1574. doi:10.1016/0016-7037(91)90128-R

Farges, F., Ponader, C.W., Calas, G., Brown, G.E., 1992. Structural environments of incompatible elements in silicate glass/melt systems: II. UIV, UV, and UVI. Geochim. Cosmochim. Acta 56, 4205–4220. doi:10.1016/0016-7037(92)90261-G

Fleet, M.E., Liu, X., Pan, Y., 2000. Rare-earth elements in chlorapatite [Ca 10 (PO 4 ) 6 Cl 2 ]: Uptake, site preference, and degradation of monoclinic structure. Am. Mineral. 85, 1437–1446. doi:10.2138/am-2000-1012

Fleet, M.E., Pan, Y., 1997. Rare earth elements in apatite: Uptake from H2O-bearing phosphate-fluoride melts and the role of volatile components. Geochim. Cosmochim. Acta 61, 4745–4760. doi:10.1016/S0016-7037(97)00292-5

Green, T.H., Adam, J., 2003. Experimentally-determined trace element characteristics of aqueous fluid from partially dehydrated mafic oceanic crust at 3.0 GPa, 650-700°C. Eur. J. Mineral. 15, 815–830. doi:10.1127/0935-1221/2003/0015-0815

Hawkesworth, C., Gallagher, K., Hergt, J., McDermott, F., 1993. Mantle and slab contribution in arc magmas. Annu. Rev. Earth Planet. Sci. 21, 175–204.

Hayden, L.A., Watson, E.B., 2007. Rutile saturation in hydrous siliceous melts and its bearing on Ti-thermometry of quartz and zircon. Earth Planet. Sci. Lett. 258, 561–568.

doi:10.1016/j.epsl.2007.04.020

Hermann, J., 2002. Allanite: thorium and light rare earth element carrier in subducted crust. Chem. Geol. 192, 289–306. doi:10.1016/S0009-2541(02)00222-X

Hermann, J., Rubatto, D., 2009. Accessory phase control on the trace element signature of sediment melts in subduction zones. Chem. Geol. 265, 512–526. doi:10.1016/j.chemgeo.2009.05.018

Hermann, J., Spandler, C.J., 2008. Sediment Melts at Sub-arc Depths: an Experimental Study. J. Petrol. 49, 717–740. doi:10.1093/petrology/egm073

Jochum, K.P., Nohl, U., 2008. Reference materials in geochemistry and environmental research and the GeoReM database. Chem. Geol. 253, 50–53. doi:10.1016/j.chemgeo.2008.04.002

Keppler, H., 2017. Fluids and trace element transport in subduction zones. Am. Mineral. 102, 5–20. doi:10.2138/am-2017-5716

Keppler, H., 1996. Constraints from partitioning experiments on the composition of subduction-zone fluids. Nature 380, 237–240. doi:10.1038/380237a0

Keppler, H., 1993. Influence of fluorine on the enrichment of high field strength trace elements in granitic rocks. Contrib. to Mineral. Petrol. 114, 479–488. doi:10.1007/BF00321752

Kessel, R., Ulmer, P., Pettke, T., Schmidt, M.W., Thompson, A.B., 2005. The water–basalt system at 4 to 6 GPa: Phase relations and second critical endpoint in a K-free eclogite at 700 to 1400 °C. Earth Planet. Sci. Lett. 237, 873–892. doi:10.1016/j.epsl.2005.06.018

Klemme, S., Dalpé, C., 2003. Trace-element partitioning between apatite and carbonatite melt. Am. Mineral. 88, 639–646. doi:10.2138/am-2003-0417

Klimm, K., Blundy, J.D., Green, T.H., 2008. Trace Element Partitioning and Accessory Phase Saturation during H2O-Saturated Melting of Basalt with Implications for Subduction Zone Chemical Fluxes. J. Petrol. 49, 523–553. doi:10.1093/petrology/egn001

Kohn, S.C., Dupont, R., Mortuza, M.G., Henderson, C.M.B., 1991. NMR evidence for five-

and six-coordinated aluminum fluoride complexes in F-bearing aluminosilicate glasses. Am. Mineral. 76, 309–312.

Konzett, J., Frost, D.J., 2009. The High P-T Stability of Hydroxyl-apatite in Natural and Simplified MORB--an Experimental Study to 15 GPa with Implications for Transport and Storage of Phosphorus and Halogens in Subduction Zones. J. Petrol. 50, 2043–2062. doi:10.1093/petrology/egp068

Kress, V.C., Carmichael, I.S.E., 1991. The compressibility of silicate liquids containing Fe2O3 and the effect of composition, temperature, oxygen fugacity and pressure on their redox states. Contrib. to Mineral. Petrol. 108, 82–92. doi:10.1007/BF00307328

Li, H., 2012. Apatite as an indicator of fluid salinity in subduction zone settings: implications for the deep earth chlorine cycle. Australian National University.

Li, H., Hermann, J., 2017. Chlorine and fluorine partitioning between apatite and sediment melt at 2.5 GPa, 800 °C: A new experimentally derived thermodynamic model. Am. Mineral. 102, 580–594. doi:10.2138/am-2017-5891

Li, H., Hermann, J., 2015. Apatite as an indicator of fluid salinity: An experimental study of chlorine and fluorine partitioning in subducted sediments. Geochim. Cosmochim. Acta 166, 267–297. doi:10.1016/j.gca.2015.06.029

Louvel, M., Sanchez-Valle, C., Malfait, W.J., Testemale, D., Hazemann, J., 2013. Zr complexation in high pressure fluids and silicate melts and implications for the mobilization of HFSE in subduction zones. Geochim. Cosmochim. Acta 104, 281–299. doi:10.1016/j.gca.2012.11.001

Mann, U., Schmidt, M.W., 2015. Melting of pelitic sediments at subarc depths: 1. Flux vs. fluid-absent melting and a parameterization of melt productivity. Chem. Geol. 404, 150–167. doi:10.1016/j.chemgeo.2015.02.032

Manning, C., 2004. The chemistry of subduction-zone fluids. Earth Planet. Sci. Lett. 223, 1–16. doi:10.1016/j.epsl.2004.04.030

Matsukage, K.N., Ono, S., Kawamoto, T., Kikegawa, T., 2004. The compressibility of a

natural apatite. Phys. Chem. Miner. 31, 580–584. doi:10.1007/s00269-004-0415-x

Mayanovic, R.A., Anderson, A.J., Bassett, W.A., Chou, I.-M., 2007. Synchrotron x-ray spectroscopy of Eu/HNO[sub 3] aqueous solutions at high temperatures and pressures and Nb-bearing silicate melt phases coexisting with hydrothermal fluids using a modified hydrothermal diamond anvil cell and rail assembly. Rev. Sci. Instrum. 78, 053904. doi:10.1063/1.2737748

Mayanovic, R.A., Yan, H., Anderson, A.J., Solferino, G., 2013. Investigation of the structural environment of Ta in a silicate glass and water system under high P–T conditions. J. Non. Cryst. Solids 368, 71–78. doi:10.1016/j.jnoncrysol.2013.03.011

Mysen, B.O., 2007. The solution behavior of H2O in peralkaline aluminosilicate melts at high pressure with implications for properties of hydrous melts. Geochim. Cosmochim. Acta 71, 1820–1834. doi:10.1016/j.gca.2007.01.007

Mysen, B.O., 2004. Element partitioning between minerals and melt, melt composition, and melt structure. Chem. Geol. 213, 1–16. doi:10.1016/j.chemgeo.2004.08.028

Mysen, B.O., Cody, G.D., 2001. Silicate-phosphate interactions in silicate glasses and melts: II. quantitative, high-temperature structure of P-bearing alkali aluminosilicate melts. Geochim. Cosmochim. Acta 65, 2413–2431. doi:10.1016/S0016-7037(01)00598-1

Mysen, B.O., Cody, G.D., Smith, A., 2004. Solubility mechanisms of fluorine in peralkaline and meta-aluminous silicate glasses and in melts to magmatic temperatures. Geochim. Cosmochim. Acta 68, 2745–2769. doi:10.1016/j.gca.2003.12.015

Mysen, B.O., Virgo, D., 1985. Iron-bearing silicate melts: Relations between pressure and redox equilibria. Phys. Chem. Miner. 12, 191–200. doi:10.1007/BF00311288

Nichols, G.T., Wyllie, P.J., Stern, C.R., 1994. Subduction zone melting of pelagic sediments constrained by melting experiments. Nature 371, 785–788.

Pan, Y., Fleet, M.E., 2002. Compositions of the Apatite-Group Minerals: Substitution Mechanisms and Controlling Factors. Rev. Mineral. Geochemistry 48, 13–49. doi:10.2138/rmg.2002.48.2

Pearce, N.J.G., Perkins, W.T., Westgate, J.A., Gorton, M.P., Jackson, S.E., Neal, C.R., Chenery, S.P., 1997. A Compilation of New and Published Major and Trace Element Data for NIST SRM 610 and NIST SRM 612 Glass Reference Materials. Geostand. Geoanalytical Res. 21, 115–144. doi:10.1111/j.1751-908X.1997.tb00538.x

Piilonen, P.C., Farges, F., Linnen, R.L., Brown, G.E., Pawlak, M., Pratt, A., 2006. Structural environment of Nb5+ in dry and fluid-rich (H2O, F) silicate glasses: a combined XANES and EXAFS study. Can. Mineral. 44, 775–794. doi:10.2113/gscanmin.44.3.775

Plank, T., 2005. Constraints from Thorium/Lanthanum on Sediment Recycling at Subduction Zones and the Evolution of the Continents. J. Petrol. 46, 921–944. doi:10.1093/petrology/egi005

Plank, T., Cooper, L.B., Manning, C.E., 2009. Emerging geothermometers for estimating slab surface temperatures. Nat. Geosci. 2, 611–615. doi:10.1038/ngeo614

Plank, T., Langmuir, C.H., 1998. The chemical composition of subducting sediment and its consequences for the crust and mantle. Chem. Geol. 145, 325–394. doi:10.1016/S0009-2541(97)00150-2

Plank, T., Langmuir, C.H., 1993. Tracing trace elements from sediment input to volcanic output at subduction zones. Nature 362, 739–746. doi:10.1038/362739a0

Ponader, C.W., Brown, G.E., 1989a. Rare earth elements in silicate systems: II. Interactions of La, Gd, and Yb with halogens. Geochim. Cosmochim. Acta 53, 2905–2914. doi:10.1016/0016-7037(89)90167-1

Ponader, C.W., Brown, G.E., 1989b. Rare earth elements in silicate systems: I. Effects of composition on the coordination environments of La, Gd, and Yb. Geochim. Cosmochim. Acta 53, 2893–2903. doi:10.1016/0016-7037(89)90166-X

Portnyagin, M., Hoernle, K., Plechov, P., Mironov, N., Khubunaya, S., 2007. Constraints on mantle melting and composition and nature of slab components in volcanic arcs from volatiles (H2O, S, Cl, F) and trace elements in melt inclusions from the Kamchatka Arc. Earth Planet. Sci. Lett. 255, 53–69. doi:10.1016/j.epsl.2006.12.005

Prowatke, S., Klemme, S., 2006. Trace element partitioning between apatite and silicate melts. Geochim. Cosmochim. Acta 70, 4513–4527. doi:10.1016/j.gca.2006.06.162

Rapp, J.F., Klemme, S., Butler, I.B., Harley, S.L., 2010. Extremely high solubility of rutile in chloride and fluoride-bearing metamorphic fluids: An experimental investigation. Geology 38, 323–326. doi:10.1130/G30753.1

Rubatto, D., Hermann, J., 2007. Experimental zircon/melt and zircon/garnet trace element partitioning and implications for the geochronology of crustal rocks. Chem. Geol. 241, 38–61. doi:10.1016/j.chemgeo.2007.01.027

Rudnick, R.L., Gao, S., 2003. Composition of the Continental Crust, in: Treatise on Geochemistry. Elsevier, pp. 1–64. doi:10.1016/B0-08-043751-6/03016-4

Sandland, T.O., Du, L.-S., Stebbins, J.F., Webster, J.D., 2004. Structure of Cl-containing silicate and aluminosilicate glasses: A 35Cl MAS-NMR study. Geochim. Cosmochim. Acta 68, 5059–5069. doi:10.1016/j.gca.2004.07.017

Scambelluri, M., Müntener, O., Ottolini, L., Pettke, T.T., Vannucci, R., 2004. The fate of B, Cl and Li in the subducted oceanic mantle and in the antigorite breakdown fluids. Earth Planet. Sci. Lett. 222, 217–234. doi:10.1016/j.epsl.2004.02.012

Schaller, T., Dingwell, D.B., Keppler, H., Knoller, W., Merwin, L., Sebald, A., 1992. Fluorine in silicate glasses: A multinuclear nuclear magnetic resonance study. Geochim. Cosmochim. Acta 56, 701–707. doi:10.1016/0016-7037(92)90091-V

Schmidt, C., Rickers, K., Bilderback, D.H., Huang, R., 2007. In situ synchrotron-radiation XRF study of REE phosphate dissolution in aqueous fluids to 800 °C. Lithos 95, 87–102. doi:10.1016/j.lithos.2006.07.017

Schmidt, M.W., 2015. Melting of pelitic sediments at subarc depths: 2. Melt chemistry, viscosities and a parameterization of melt composition. Chem. Geol. 404, 168–182. doi:10.1016/j.chemgeo.2015.02.013

Schmidt, M.W., Vielzeuf, D., Auzanneau, E., 2004. Melting and dissolution of subducting crust at high pressures: the key role of white mica. Earth Planet. Sci. Lett. 228, 65–84.

doi:10.1016/j.epsl.2004.09.020

Skora, S., Blundy, J., 2012. Monazite solubility in hydrous silicic melts at high pressure conditions relevant to subduction zone metamorphism. Earth Planet. Sci. Lett. 321-322, 104–114. doi:10.1016/j.epsl.2012.01.002

Skora, S., Blundy, J., 2010. High-pressure Hydrous Phase Relations of Radiolarian Clay and Implications for the Involvement of Subducted Sediment in Arc Magmatism. J. Petrol. 51, 2211–2243. doi:10.1093/petrology/egq054

Skora, S., Blundy, J.D., Brooker, R.A., Green, E.C.R., de Hoog, J.C.M., Connolly, J.A.D., 2015. Hydrous Phase Relations and Trace Element Partitioning Behaviour in Calcareous Sediments at Subduction-Zone Conditions. J. Petrol. 56, 953–980. doi:10.1093/petrology/egv024

Spandler, C., Hermann, J., Arculus, R., Mavrogenes, J., 2003. Redistribution of trace elements during prograde metamorphism from lawsonite blueschist to eclogite facies; implications for deep subduction-zone processes. Contrib. to Mineral. Petrol. 146, 205–222. doi:10.1007/s00410-003-0495-5

Spandler, C., Mavrogenes, J., Hermann, J., 2007. Experimental constraints on element mobility from subducted sediments using high-P synthetic fluid/melt inclusions. Chem. Geol. 239, 228–249. doi:10.1016/j.chemgeo.2006.10.005

Spandler, C., Yaxley, G., Green, D.H., Scott, D., 2010. Experimental phase and melting relations of metapelite in the upper mantle: Implications for the petrogenesis of intraplate magmas. Contrib. to Mineral. Petrol. 160, 569–589. doi:10.1007/s00410-010-0494-2

Stebbins, J.F., 2016. Glass structure, melt structure, and dynamics: Some concepts for petrology. Am. Mineral. 101, 753–768. doi:10.2138/am-2016-5386

Stebbins, J.F., 1987. Identification of multiple structural species in silicate glasses by 29Si NMR. Nature 330, 465–467. doi:10.1038/330465a0

Stepanov, A.S., Hermann, J., Rubatto, D., Rapp, R.P., 2012. Experimental study of

monazite/melt partitioning with implications for the REE, Th and U geochemistry of crustal rocks. Chem. Geol. 300-301, 200–220. doi:10.1016/j.chemgeo.2012.01.007

Stolper, E., Newman, S., 1994. The role of water in the petrogenesis of Mariana trough magmas. Earth Planet. Sci. Lett. 121, 293–325. doi:10.1016/0012-821X(94)90074-4

Sun, S. -s., McDonough, W.F., 1989. Chemical and isotopic systematics of oceanic basalts: implications for mantle composition and processes. Geol. Soc. London, Spec. Publ. 42, 313–345. doi:10.1144/GSL.SP.1989.042.01.19

Tanis, E.A., Simon, A., Zhang, Y., Chow, P., Xiao, Y., Hanchar, J.M., Tschauner, O., Shen, G., 2016. Rutile solubility in NaF–NaCl–KCl-bearing aqueous fluids at 0.5–2.79GPa and 250–650°C. Geochim. Cosmochim. Acta 177, 170–181. doi:10.1016/j.gca.2016.01.003

Thomsen, T.B., Schmidt, M.W., 2008. Melting of carbonated pelites at 2.5–5.0 GPa, silicate–carbonatite liquid immiscibility, and potassium–carbon metasomatism of the mantle. Earth Planet. Sci. Lett. 267, 17–31. doi:10.1016/j.epsl.2007.11.027

Tropper, P., Manning, C.E., Harlov, D.E., 2013. Experimental determination of CePO 4 and YPO 4 solubilities in H 2 O-NaF at 800°C and 1 GPa: implications for rare earth element transport in high-grade metamorphic fluids. Geofluids 13, 372–380. doi:10.1111/gfl.12031

Tropper, P., Manning, C.E., Harlov, D.E., 2011. Solubility of CePO4 monazite and YPO4 xenotime in H2O and H2O–NaCl at 800°C and 1GPa: Implications for REE and Y transport during high-grade metamorphism. Chem. Geol. 282, 58–66. doi:10.1016/j.chemgeo.2011.01.009

Tsay, A., Zajacz, Z., Sanchez-Valle, C., 2014. Efficient mobilization and fractionation of rare-earth elements by aqueous fluids upon slab dehydration. Earth Planet. Sci. Lett. 398, 101–112. doi:10.1016/j.epsl.2014.04.042

Tsay, A., Zajacz, Z., Ulmer, P., Sanchez-Valle, C., 2017. Mobility of major and trace elements in the eclogite-fluid system and element fluxes upon slab dehydration.

Geochim. Cosmochim. Acta 198, 70–91. doi:10.1016/j.gca.2016.10.038

Tsuno, K., Dasgupta, R., 2012. The effect of carbonates on near-solidus melting of pelite at 3GPa: Relative efficiency of H2O and CO2 subduction. Earth Planet. Sci. Lett. 319-320, 185–196. doi:10.1016/j.epsl.2011.12.007

Tsuno, K., Dasgupta, R., 2011. Melting phase relation of nominally anhydrous, carbonated pelitic-eclogite at 2.5–3.0 GPa and deep cycling of sedimentary carbon. Contrib. to Mineral. Petrol. 161, 743–763. doi:10.1007/s00410-010-0560-9

Wallace, P.J., 2005. Volatiles in subduction zone magmas: concentrations and fluxes based on melt inclusion and volcanic gas data. J. Volcanol. Geotherm. Res. 140, 217–240. doi:10.1016/j.jvolgeores.2004.07.023

Watson, E.B., Capobianco, C.J., 1981. Phosphorus and the rare earth elements in felsic magmas: an assessment of the role of apatite. Geochim. Cosmochim. Acta 45, 2349–2358. doi:10.1016/0016-7037(81)90088-0

Watson, E.B., Green, T.H., 1981. Apatite/liquid partition coefficients for the rare earth elements and strontium. Earth Planet. Sci. Lett. 56, 405–421. doi:10.1016/0012-821X(81)90144-8

Wood, B.J., Blundy, J.D., 2014. Trace Element Partitioning: The Influences of Ionic Radius, Cation Charge, Pressure, and Temperature, in: Treatise on Geochemistry. Elsevier, pp. 421–448. doi:10.1016/B978-0-08-095975-7.00209-6

Zeng, Q., Stebbins, J.F., 2000. Fluoride sites in aluminosilicate glasses: High-resolution 19F NMR results. Am. Mineral. 85, 863–867. doi:10.1029/2007GL031617

**Figure Captions**

Fig 1 Representative BSE images showing the mineral assemblage and quench textures of 2.5 GPa, 800°C experiments. (a) Major minerals garnet, phengite, quartz, kyanite and accessory minerals apatite, rutile, zircon, coexist with quenched melt from exp. C3269. (b) Accessory phases apatite, rutile and zircon with small grain sizes of 1-5 μm, randomly distributed in bubble-free quenched melt from exp. C4049.

Fig 2 Mixed analyses of melt and apatite by LA-ICPMS were used to derive the REE, Y, Sr, Th and U contents in apatite. Data shown are from exp. C3922. Linear correlations were established between the concentrations of trace elements and P, with the slope representing the ratio of a given trace element/P in apatite.

Fig 3 Trace element compositions of melt normalized to the starting composition. The melt Cl and F contents (in ppm) are given in brackets following the sample number. C1846 is a F, Cl-free EPSM experiment from Hermann and Rubatto (2009). Recalculated Th, La, Ce, Pr, Nd and Sm normalized melt concentrations for exp. C3922 (C3922* W/C) after adjusting the apatite mass fraction for a GLOSS composition, are also plotted. Such a calculation was performed using equation (3) and apatite-melt partition coefficients obtained for exp. C3922, based on the assumption that melt and apatite take up the entire budget of the trace element in question.

Fig 4 Trace element concentrations in melt are plotted against melt fraction (a), mica mass fraction (b) and melt Cl content (c-h) in three data groups based on the bulk Cl and F contents: “Cl”, “Cl+700ppmF” and “Cl+1500ppmF”. The anomalous data point from exp. C3922 in (d) can be explained by the high Ce content in apatite, see section 3.2 for details. The anomalous data points from exp. D1222 in (d), and from exp. C3269 and D1218 in (e) possibly result from anomalies in their bulk compositions.

Fig 5 (a) In comparison to the allanite-buffered melt composition of exp. 1846 from Hermann and Rubatto (2009), REE diagrams for melt compositions in this study display a steep decrease from LREE towards MREE, with a positive Eu anomaly, demonstrating the apatite control on LMREE partitioning. The melt Cl and F contents (in ppm) are given in brackets following the sample number. (b) LMREE contents in melt show an increase with the Cl content in melt, while the concentrations of HREE, Y and Sc show an initial increase followed by a decrease (c).

Fig 6 Concentrations of HFSE (Nb, Ta, Zr and Hf) decrease with the F+Cl content in melt.

Fig 7 All but experiments C3922 and C3955 have uniform $Th_N/U_N$ (a) and $Th_N/La_N$ (b) melt ratios, which are similar to those observed in the allanite-buffered melt of exp. C1846 from Hermann and Rubatto (2009). The higher $Th_N/U_N$ and $Th_N/La_N$ ratios for exp. C3922 and C3955, reflect greater apatite contribution to Th and U partitioning, in contrast to the dominant allanite control for all other experiments. The near constant $Sm_N/La_N$ ratios (c) for apatite-buffered melts of this study are lower than the allanite-buffered melt of exp. C1846. $Ce_N/Nb_N$ (d), $Ce_N/Y_N$ (e) and $Zr_N/Nb_N$ (f) ratios for melt display increasing trends with Cl in melt, demonstrating the Cl effect on the fractionation between LMREE (Ce), HREE (Y) and HFSE (Zr, Nb). The anomalous data points in (d) and (e) correspond to the anomalous data points in Fig. 4d and 4e. The calculated $Ce_N/Y_N$ ratio for exp. C1846 is unusually high, as the reported bulk Y content for exp. 1846 is about two times that of the bulk Y for experiments in this study, despite the similar absolute Y concentrations in melt.

Fig 8 Sr (a), Th, U (b) and LMREE (c) contents in apatite show an increase with the mole fraction of ClAp ($X_{Cl}^{Ap}$). The relative increase between exp. C3927 with 0 $X_{Cl}^{Ap}$ and exp. C3922 with 0.4 $X_{Cl}^{Ap}$ is positively correlated with cation radius and charge (c). Note that the Th and U contents in apatite from exp. C4059 ($X_{Cl}^{Ap}$ =0.075) were used in the calculation for Th and U, as the contents in exp. C3927 were not constrained.

Fig 9 $Th_N/U_N$ (a) and $Th_N/La_N$ (b) ratios for apatite show positive correlations with the mole fraction of ClAp ($X_{Cl}^{Ap}$); while the $Sm_N/La_N$ (c) ratio shows a negative correlation with $X_{Cl}^{Ap}$. These correlations demonstrate the relative sensitivity of these elements to the increase of $X_{Cl}^{Ap}$, i.e., Th>U, Th>La and Sm<La.

Fig 10 LMREE partition coefficients between apatite and melt show a concave pattern. HREE partition coefficients for exp. C3269, D1218 and C3922 are well constrained, and form the right limb of the concave pattern. Selected trace element partition coefficients between apatite and melt reported in previous experimental studies of Prowatke and Klemme (2006), Watson and Green (1981), Klemme and Dalpé (2003), Fleet and Pan (1997) and Fleet et al. (2000) are also plotted for comparison, see section 4.3 for details.

Fig. 11 Variations of trace element partition coefficients between apatite and melt are shown in plots vs Cl content in melt or mole fraction of ClAp ($X_{Cl}^{Ap}$), with La, Sm (a), Sr (b) and Th, U (c) given as examples; supporting the trends observed for trace element concentrations in apatite vs. $X_{Cl}^{Ap}$, and the trace element concentrations in melt vs. Cl in melt.

Fig 12 REE (excluding Eu) and Y partition coefficients between apatite and melt were fitted to the lattice strain model of Blundy and Wood (1994). Regressions results for exp. D1218 are shown as an example, (a) fitting LREE and REE data respectively, with VII coordinated ionic radii, (b) fitting LREE and HREE data respectively, with IX coordinated ionic radii. The fitted values for Young's modulus ($E$) show a subtle increase with the mole fraction of ClAp (c). As shown by the regression results for exp. D 1218, the $E$ value from fitting all REE can be considered as the weighted mean of the values from fitting LREE and HREE data.

**Fig. 1**

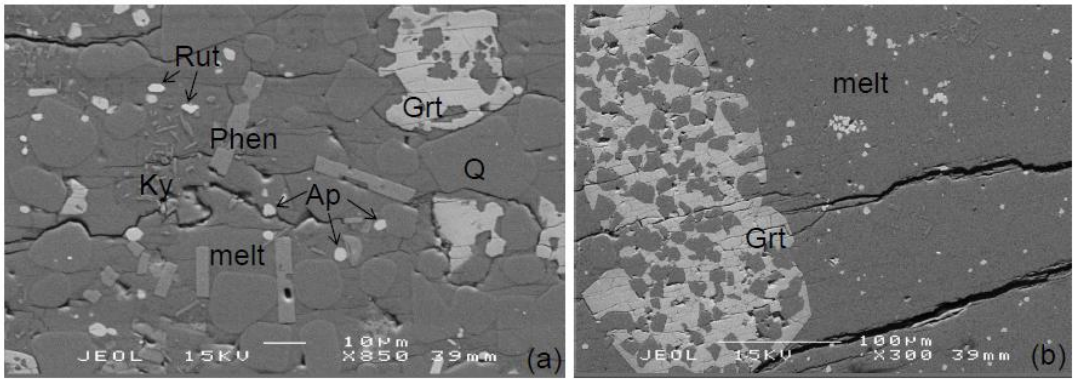

**Fig. 2**

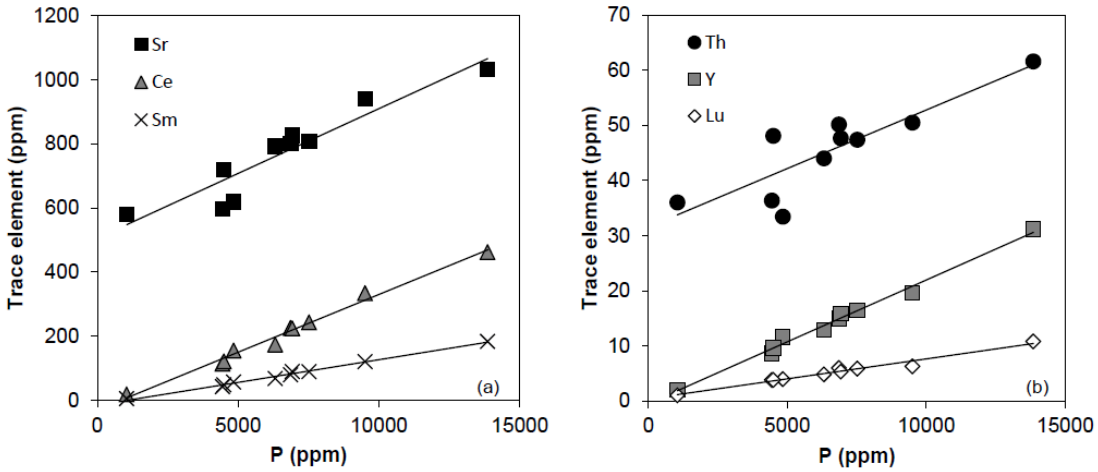

**Fig. 3**

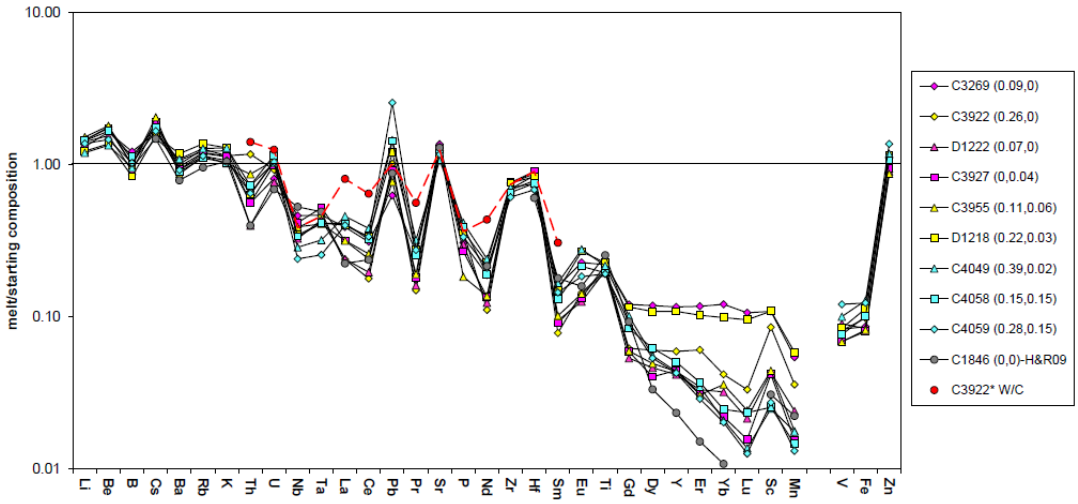

**Fig. 4**

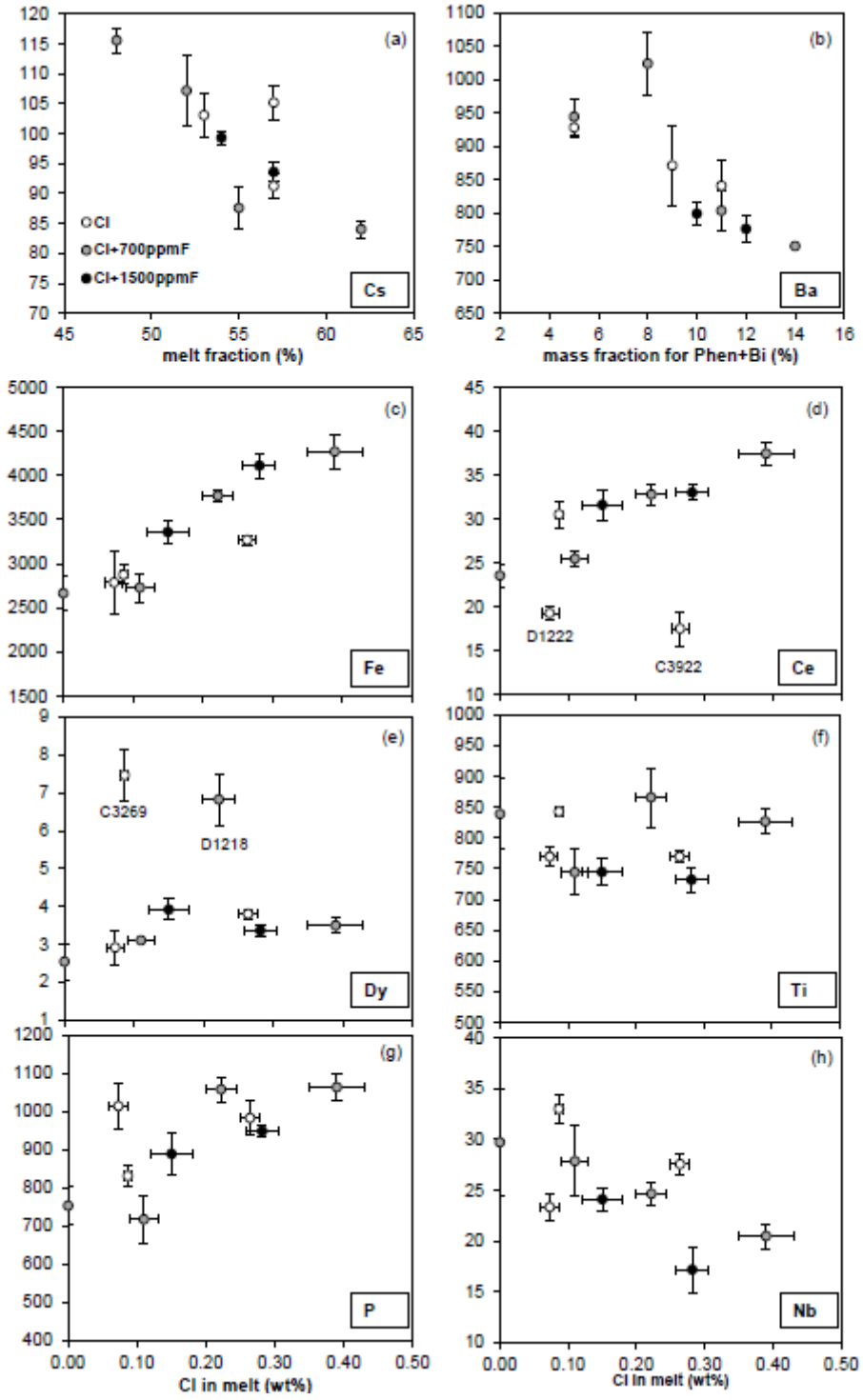

**Fig. 5**

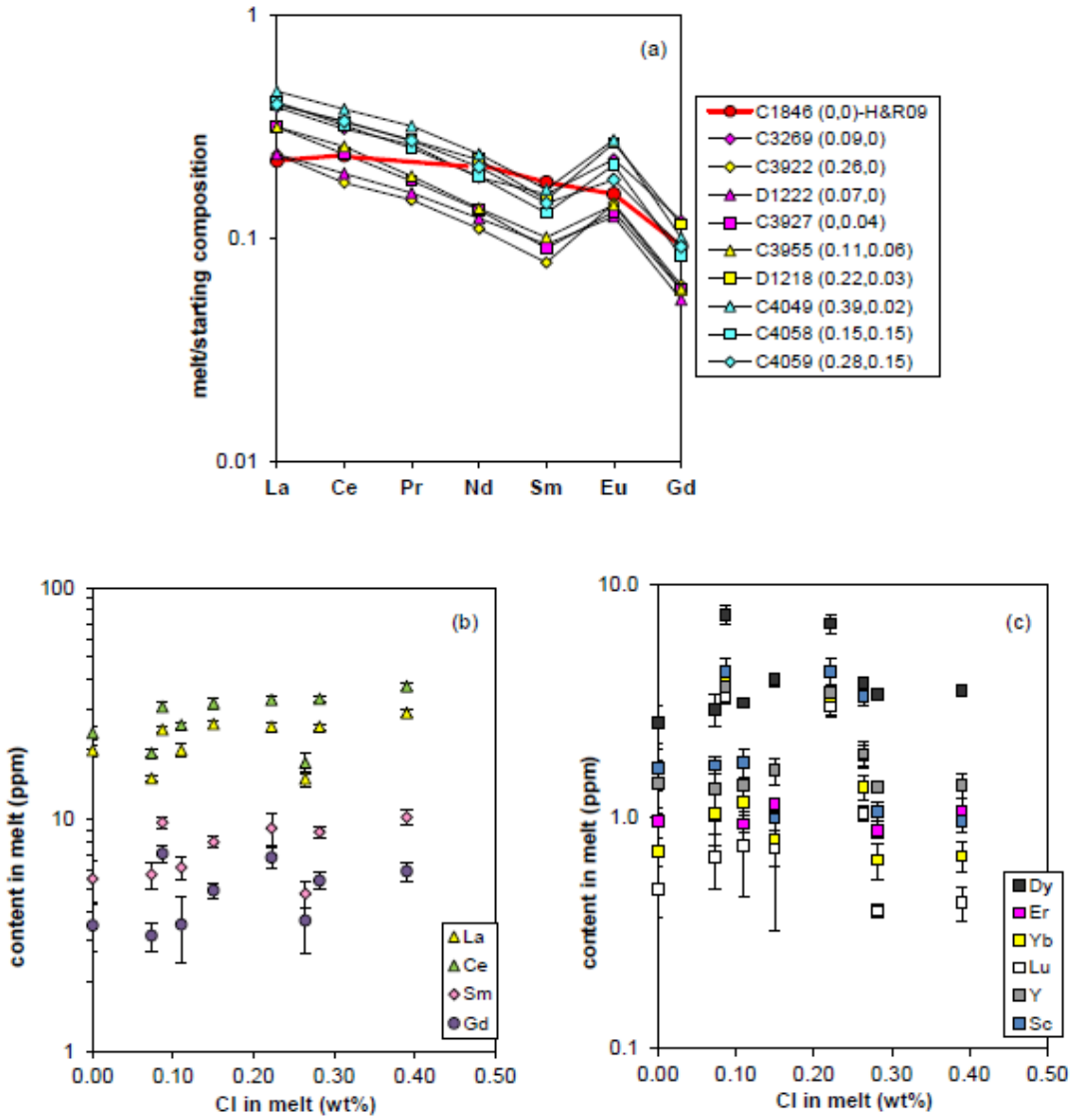

**Fig. 6**

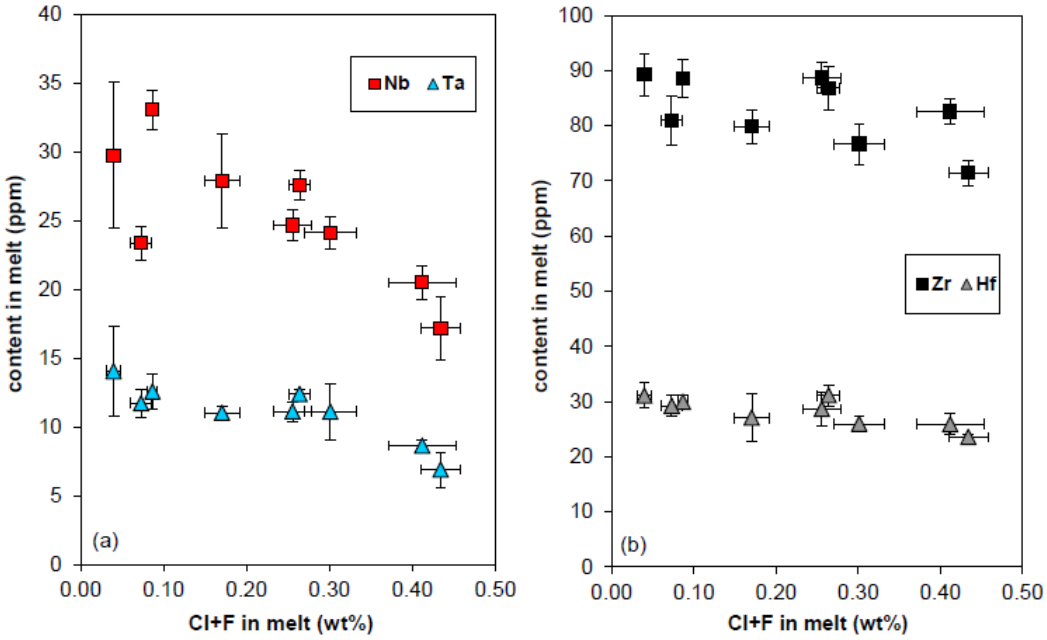

**Fig. 7**

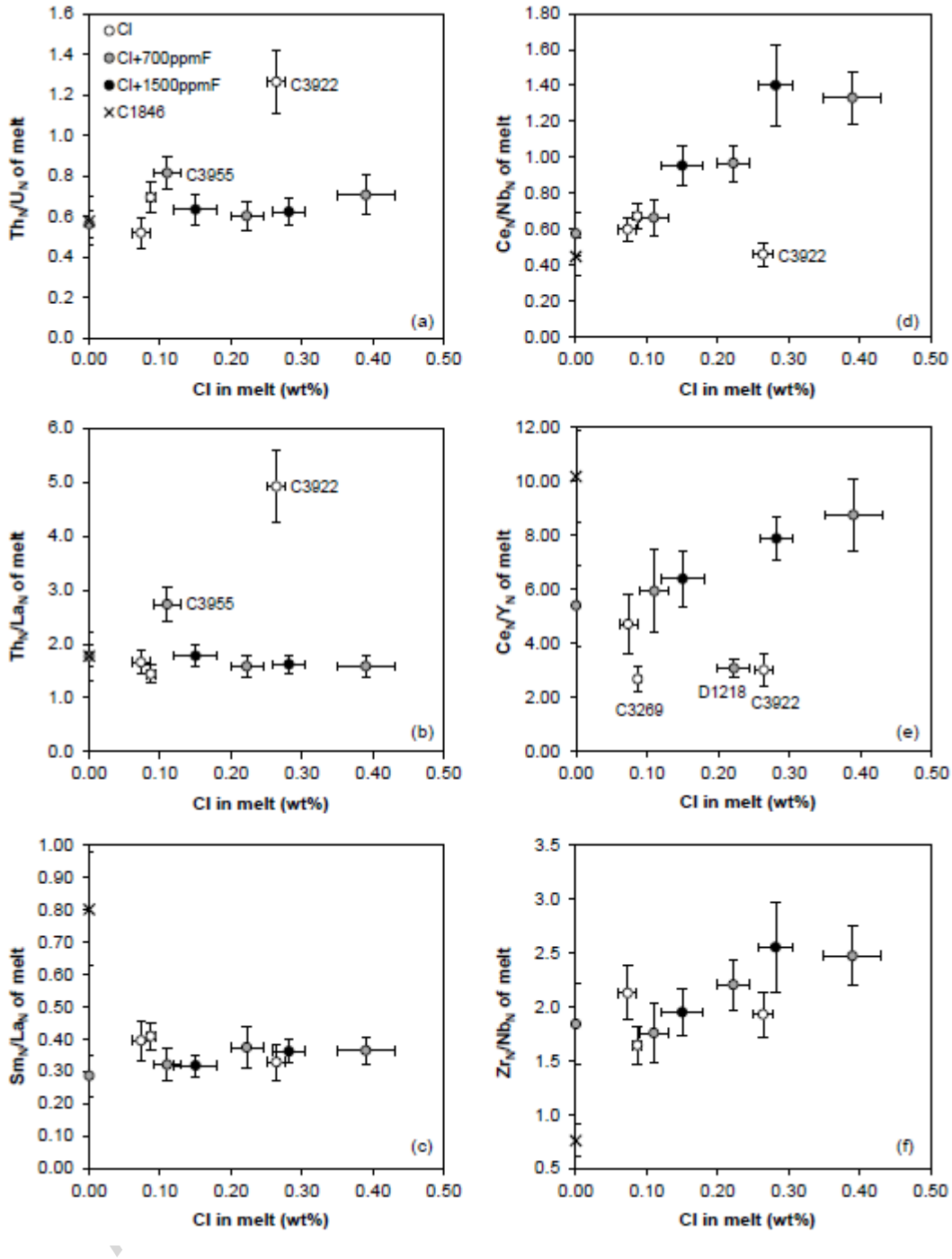

**Fig. 8**

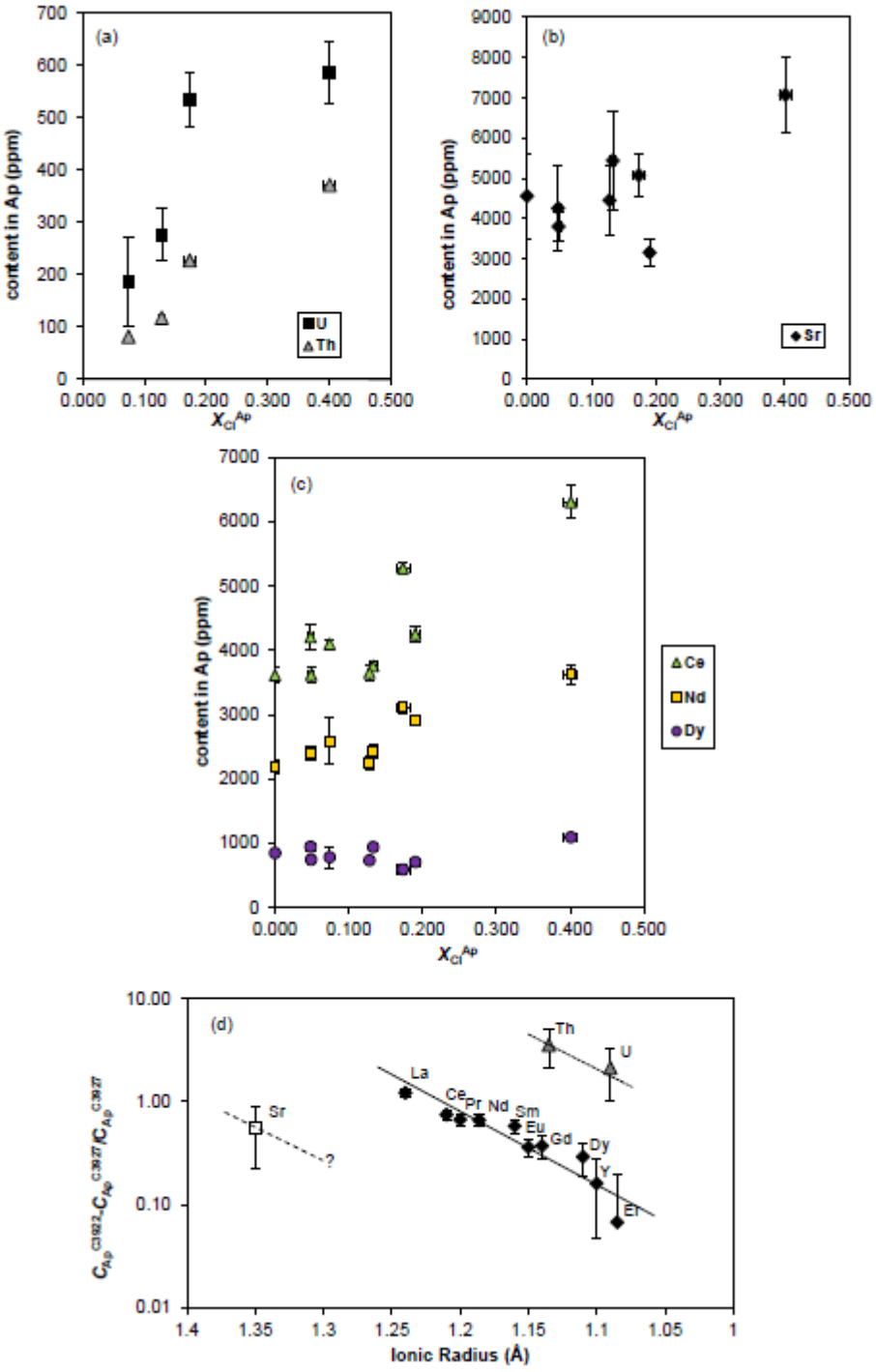

**Fig. 9**

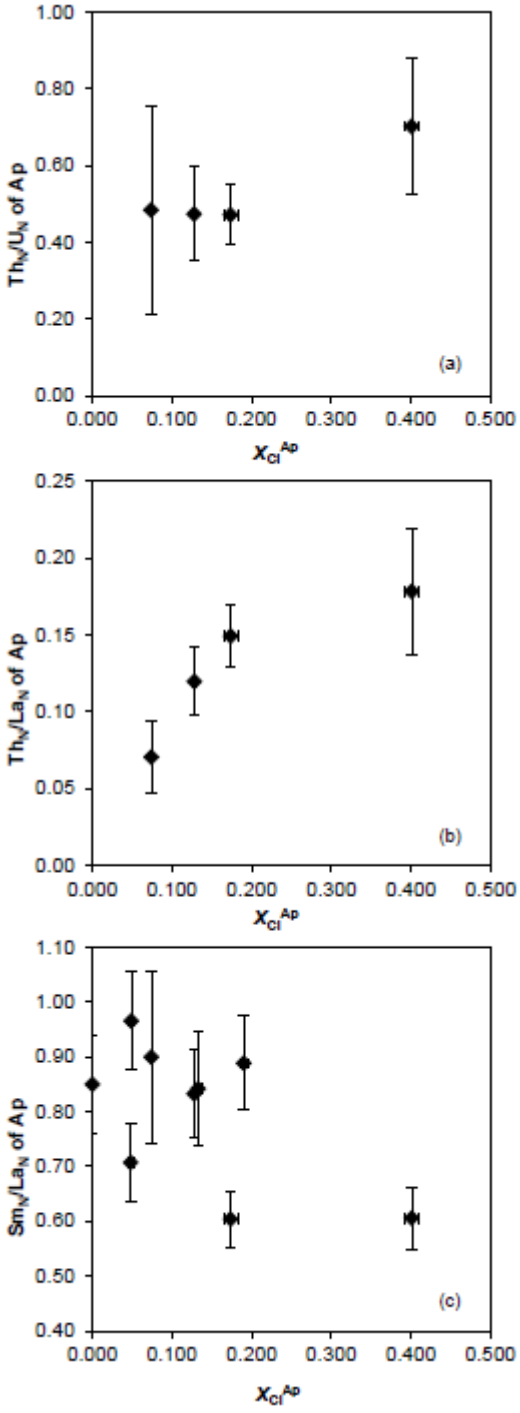

**Fig. 10**

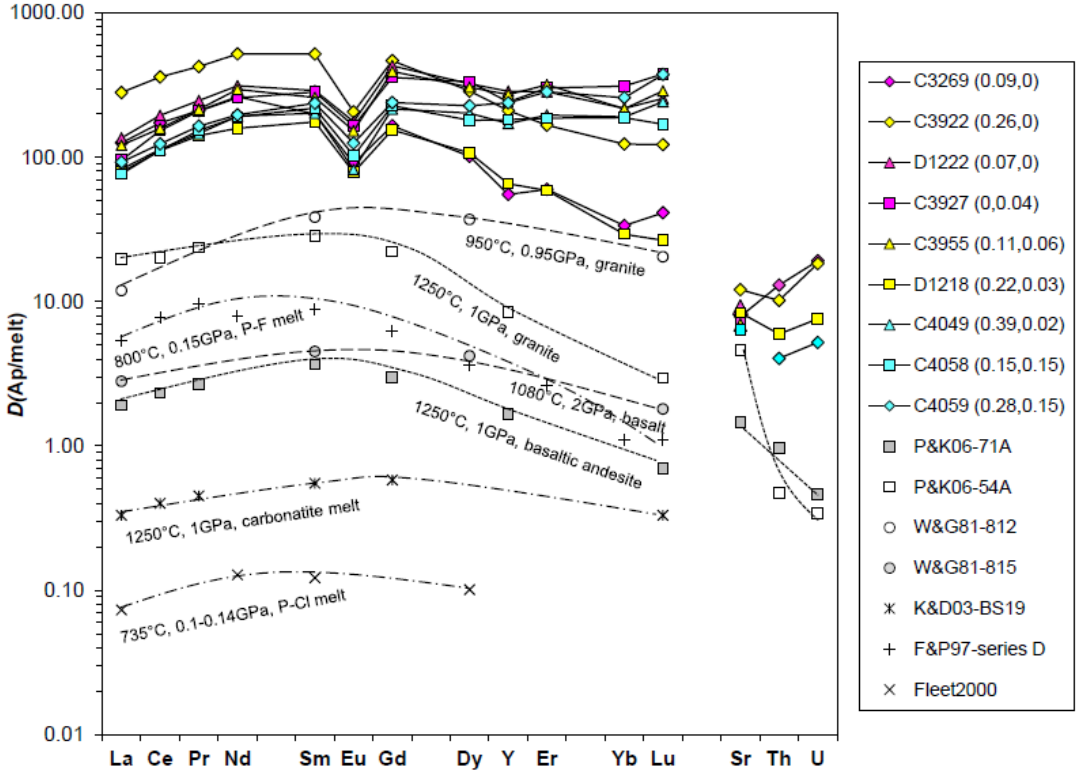

**Fig. 11**

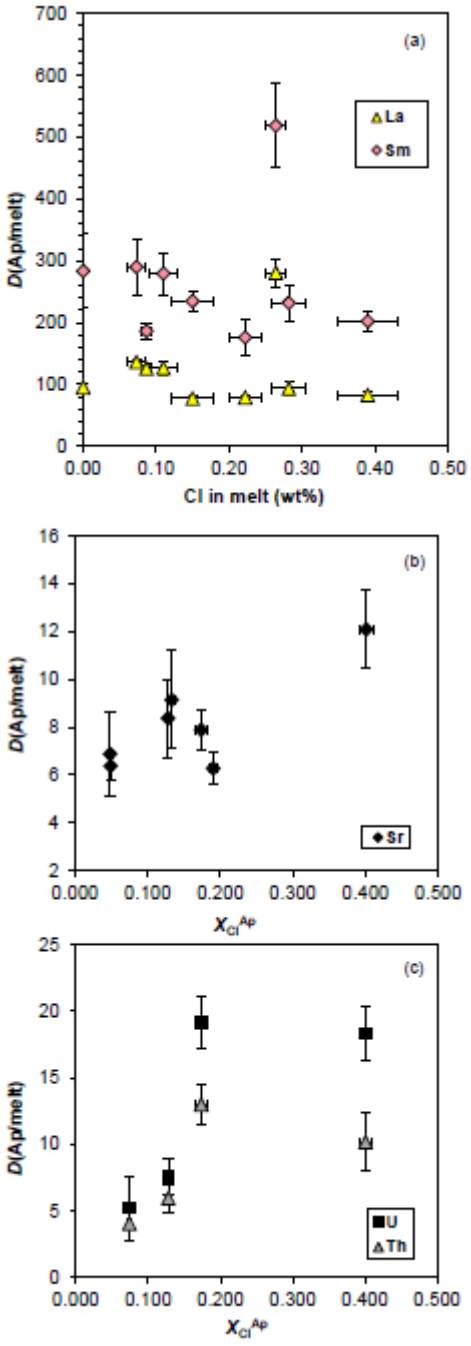

**Fig. 12**

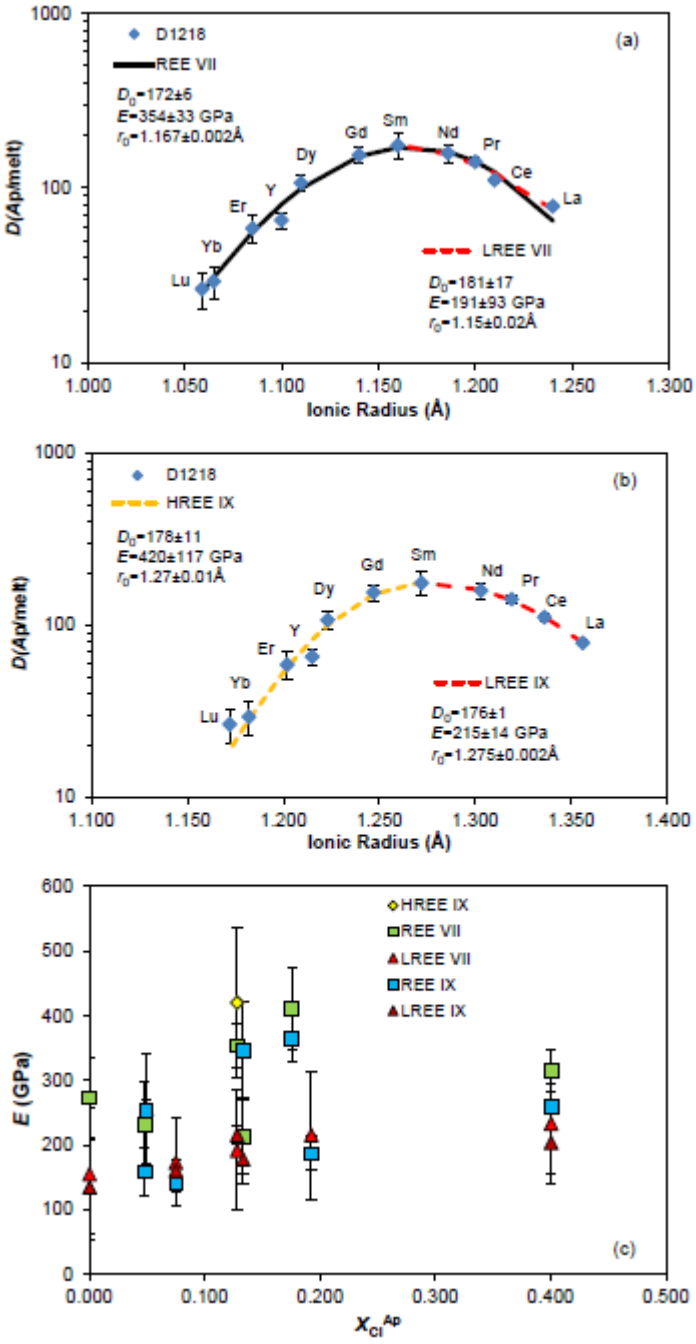

Table 1 Major and trace element compositions of EPSM and their comparison to GLOSS (Plank and Langmuir, 1998) and upper continental crust (Rudnick and Gao, 2003).

| | EPSM | | GLOSS | | UCC |
|---|---|---|---|---|---|
| wt% | | | (P&L98) | | (R&G03) |
| $SiO_2$ | 63.56 | | 58.57 | | 66.62 |
| $TiO_2$ | 0.62 | | 0.62 | | 0.64 |
| $Al_2O_3$ | 13.57 | | 11.91 | | 15.4 |
| FeO | 4.31 | | 5.21 | | 5.04 |
| MnO | 0.10 | | 0.32 | | 0.1 |
| MgO | 2.32 | | 2.48 | | 2.48 |
| CaO | 2.26 | | 5.95 | | 3.59 |
| $Na_2O$ | 2.42 | | 2.43 | | 3.27 |
| $K_2O$ | 2.71 | | 2.04 | | 2.8 |
| $P_2O_5$ | 0.92 | | 0.19 | | 0.15 |
| $H_2O$ | 7.20 | | 7.29 | | |
| F (ppm) | | | | | 557 |
| Tot. | 100 | | 97.01 | | 100.09 |
| ppm | | *σ* | | *σ* | |
| Li | 37 | *1.0* | | | 21 |
| Be | 6 | *0.2* | | | 2.1 |
| B | 166 | *3.3* | | | 17 |
| Sc | 39 | *2.1* | 13.1 | *1.03* | 14 |
| Ti | 3833 | *135* | | | |
| V | 95 | *4.5* | 110 | *10.7* | 97 |
| Mn | 1228 | *38.6* | | | |
| Zn | 76 | *13* | 86.4 | *8.88* | 67 |
| Rb | 64 | *0.9* | 57.2 | *6.66* | 84 |
| Sr | 471 | *33* | 327 | *53.8* | 320 |
| Y | 32 | *1.8* | 29.8 | *9.92* | 21 |
| Zr | 117 | *8* | 130 | *8.5* | 193 |
| Nb | 72 | *4.2* | 8.94 | *0.94* | 12 |
| Cs | 56 | *1.0* | 3.48 | *0.5* | 4.9 |
| Ba | 867 | *66* | 776 | *137.1* | 624 |
| La | 63 | *3.4* | 28.8 | *6.8* | 31 |
| Ce | 98 | *5.9* | 57.3 | *10.3* | 63 |
| Pr | 57 | *3.7* | | | 7.1 |
| Nd | 63 | *3.9* | 27 | *8.3* | 27 |
| Sm | 61 | *3.7* | 5.78 | *1.83* | 4.7 |
| Eu | 58 | *3.6* | 1.31 | *0.44* | 1 |
| Gd | 59 | *3.5* | 5.26 | *2.04* | 4 |
| Dy | 63 | *3.7* | 4.99 | *1.86* | 3.9 |
| Er | 31 | *1.8* | 2.92 | *1.06* | 2.3 |
| Yb | 32 | *1.8* | 2.76 | *0.88* | 2 |

| | | | | | |
|---|---|---|---|---|---|
| Lu | 31 | *1.9* | 0.413 | *0.133* | 0.31 |
| Hf | 34 | *2.8* | 4.06 | *0.3* | 5.3 |
| Ta | 27 | *1.9* | 0.63 | *0.06* | 0.9 |
| Pb | 50 | *10* | 19.9 | *5.4* | 17 |
| Th | 31 | *2.3* | 6.91 | *0.8* | 10.5 |
| U | 35 | *2.0* | 1.68 | *0.18* | 2.7 |

Table 2 Trace element compositions of melt from LA-ICPMS analyses.

| Sample | C3269 | | C3922 | | D1222 | | C3927 | | C3955 | | D1218 | | C4049 | | C4058 | | C4059 | | BCR-2G | | [f]Ref |
|---|---|---|---|---|---|---|---|---|---|---|---|---|---|---|---|---|---|---|---|---|---|
| Start. Comp. | EPSM-1 | | EPSM-2 | | EPSM-6 | | EPSM-3 | | EPSM-4 | | EPSM-5 | | EPSM-8 | | EPSM-10 | | EPSM-9 | | | | |
| bulk $H_2O$ (wt%) | 6.64 | | 6.68 | | 7.02 | | 6.74 | | 6.46 | | 6.29 | | 7.16 | | 7.17 | | 7.16 | | | | |
| bulk Cl (ppm) | 800 | | 2100 | | 700 | | 0 | | 650 | | 1900 | | 3000 | | 1100 | | 2200 | | | | |
| bulk F (ppm) | 0 | | 0 | | 0 | | 700 | | 900 | | 700 | | 700 | | 1500 | | 1500 | | | | |
| [a]Major/minor minerals | Grt, Phen, Q, Ky | | Grt, Phen, Q, Ky | | Grt, Phen, Q | | Grt, Phen, Q | | Grt, Phen, Q, Bi | | Grt, Phen, Q | | Grt, Phen, Q, Ky | | Grt, Phen, Q, Bi, Ky | | Grt, Phen, Q, Bi, Ky | | | | |
| [a]Accessory. Minerals | Ap, Rut, Zir, All? | | Ap, Rut, Zir, All? | | Ap, Rut, Zir, All | | Ap, Rut, Zir, All | | Ap, Rut, Zir, All | | Ap, Rut, Zir, All | | Ap, Rut, Zir, All? | | Ap, Rut, Zir, All | | Ap, Rut, Zir, All | | | | |
| [b]Melt fraction (%) | 57 | | 57 | | 53 | | 52 | | 48 | | 55 | | 62 | | 54 | | 57 | | | | |
| [c]Cl in melt (wt%) | 0.09 | *0.01* | 0.26 | *0.01* | 0.07 | *0.01* | | | 0.11 | *0.02* | 0.22 | *0.02* | 0.39 | *0.04* | 0.15 | *0.03* | 0.28 | *0.02* | | | |
| [c]F in melt (wt%) | | | | | | | 0.04 | *0.01* | 0.06 | *0.01* | 0.034 | *0.0004* | 0.02 | *0.01* | 0.15 | *0.01* | 0.15 | *0.01* | | | |
| ppm | | *σ(7)* | | *σ(3)* | | *σ(5)* | | *σ(4)* | | *σ(3)* | | *σ(6)* | | *σ(9)* | | *σ(6)* | | *σ(9)* | | *σ(14)* | |
| Li | 48 | *0.9* | 53 | *1.1* | 52 | *1.8* | 53 | *1.8* | 56 | *0.5* | 45 | *0.4* | 44 | *0.9* | 53 | *1.4* | 50 | *1.2* | 9 | *0.5* | |
| Be | 9 | *0.1* | 10 | *0.4* | 9 | *0.3* | 10 | *0.4* | 10 | *0.1* | 8 | *0.2* | 7 | *0.3* | 9 | *0.3* | 8 | *0.1* | 0.2 | *0.01* | |
| B | 130 | *6.2* | 115 | *7.5* | 97 | *7.4* | 106 | *9.4* | 105 | *11.8* | 89 | *7.6* | 101 | *6.4* | 121 | *7.8* | 109 | *4.3* | | | |
| P | 832 | *27* | 983 | *44* | 1014 | *62* | 753 | *48* | 718 | *62* | 1058 | *32* | 1064 | *36* | 889 | *56* | 949 | *16* | 1237 | *43.1* | 1615 |
| Sc | 4 | *0.6* | 3 | *0.3* | 2 | *0.1* | 2 | *0.3* | 2 | *0.2* | 4 | *0.6* | 1 | *0.1* | 1 | *0.1* | 1 | *0.1* | 28 | *0.6* | 33 |
| Ti | 843 | *9* | 770 | *9* | 769 | *15* | 839 | *57* | 744 | *37* | 866 | *48* | 827 | *19* | 744 | *22* | 732 | *20* | 11599 | *284* | 13605 |
| V | 8 | *0.5* | 8 | *0.3* | 9 | *0.6* | 7 | *0.3* | 6 | *1* | 8 | *0.8* | 10 | *1.1* | 7 | *1.3* | 11 | *1.3* | 396 | *12.5* | 425 |
| Mn | 66 | *1.7* | 44 | *0.2* | 29 | *1.8* | 19 | *1.4* | 22 | *0.8* | 72 | *1.8* | 22 | *1* | 18 | *0.4* | 16 | *0.4* | 1458 | *38.5* | 1550 |
| Fe | 2876 | *111* | 3269 | *52* | 2788 | *360* | 2666 | *199* | 2730 | *162* | 3771 | *71* | 4270 | *189* | 3360 | *132* | 4110 | *140* | 92932 | *3527* | 97222 |
| Zn | 68 | *3* | 84 | *8* | 68 | *5* | 71 | *8* | 66 | *2* | 88 | *5* | 89 | *5* | 81 | *6* | 103 | *2* | 183 | *10* | 125 |
| Rb | 78 | *2.6* | 81 | *4.6* | 77 | *1.9* | 76 | *3.2* | 73 | *1.7* | 88 | *2.5* | 82 | *1.5* | 71 | *1* | 73 | *1.8* | 46 | *1.4* | 47 |

| | | | | | | | | | | | | | | | | | | | | |
|---|---|---|---|---|---|---|---|---|---|---|---|---|---|---|---|---|---|---|---|---|
| Sr | 643 | *15* | 585 | *21* | 595 | *18* | 599 | *26* | 618 | *10* | 531 | *19* | 502 | *16* | 595 | *12* | 550 | *10* | 296 | *9* | 342 |
| Y | 3.7 | *0.6* | 1.9 | *0.2* | 1.3 | *0.3* | 1.4 | *0.4* | 1.4 | *0.3* | 3.4 | *0.2* | 1.4 | *0.2* | 1.6 | *0.2* | 1.3 | *0.1* | 28 | *1* | 35 |
| Zr | 89 | *3* | 87 | *4* | 81 | *4* | 89 | *4* | 80 | *3* | 89 | *3* | 83 | *2* | 77 | *4* | 71 | *2* | 153 | *6* | 184 |
| Nb | 33 | *1.4* | 28 | *1.1* | 23 | *1.2* | 30 | *5.3* | 28 | *3.5* | 25 | *1.1* | 20 | *1.2* | 24 | *1.1* | 17 | *2.3* | 9.2 | *0.2* | 12.5 |
| Cs | 91 | *2.1* | 105 | *2.8* | 103 | *3.6* | 107 | *5.8* | 116 | *2* | 88 | *3.5* | 84 | *1.4* | 99 | *1.1* | 94 | *1.6* | 1 | *0.1* | 1.16 |
| Ba | 928 | *16* | 871 | *61* | 841 | *39* | 804 | *31* | 750 | *1* | 1024 | *47* | 944 | *27* | 776 | *20* | 799 | *17* | 568 | *28* | 683 |
| La | 24 | *0.8* | 15 | *1.1* | 15 | *0.4* | 20 | *1.1* | 20 | *1.4* | 25 | *0.9* | 29 | *1.3* | 26 | *0.9* | 25 | *0.7* | 21 | *0.5* | 24.7 |
| Ce | 31 | *1.6* | 18 | *1.9* | 19 | *0.7* | 24 | *1.3* | 25 | *0.8* | 33 | *1.2* | 37 | *1.3* | 32 | *1.8* | 33 | *0.9* | 45 | *2.1* | 53.3 |
| Pr | 15 | *0.3* | 8 | *1.0* | 9 | *0.6* | 10 | *0.7* | 11 | *0.3* | 16 | *0.6* | 18 | *0.7* | 14 | *0.3* | 16 | *0.3* | 5.6 | *0.3* | 6.7 |
| Nd | 12 | *1.5* | 7 | *0.3* | 8 | *1.1* | 8 | *0.8* | 9 | *1.2* | 14 | *1.5* | 15 | *0.8* | 12 | *0.5* | 13 | *0.6* | 25 | *1.3* | 28.9 |
| Sm | 10 | *0.6* | 5 | *0.6* | 6 | *0.7* | 6 | *1.1* | 6 | *0.7* | 9 | *1.4* | 10 | *0.7* | 8 | *0.5* | 9 | *0.5* | 5.8 | *0.5* | 6.59 |
| Eu | 13 | *0.7* | 8 | *0.7* | 7 | *0.6* | 8 | *0.3* | 8 | *0.2* | 15 | *0.4* | 16 | *0.8* | 12 | *1.0* | 11 | *0.4* | 1.6 | *0.1* | 1.97 |
| Gd | 7.1 | *0.6* | 3.7 | *1.0* | 3.1 | *0.4* | 3.5 | *0.8* | 3.5 | *1.1* | 6.8 | *0.7* | 6 | *0.6* | 4.9 | *0.4* | 5.4 | *0.4* | 5.2 | *0.3* | 6.71 |
| Dy | 7.5 | *0.7* | 3.8 | *0.1* | 2.9 | *0.4* | 2.5 | *0.5* | 3.1 | *0.02* | 6.8 | *0.7* | 3.5 | *0.2* | 3.9 | *0.3* | 3.4 | *0.2* | 5.5 | *0.3* | 6.44 |
| Er | 3.6 | *0.3* | 1.8 | *0.2* | 1.0 | *0.3* | 1.0 | *0.1* | 0.9 | *0.1* | 3.1 | *0.3* | 1.1 | *0.2* | 1.1 | *0.1* | 0.9 | *0.1* | 2.9 | *0.2* | 3.7 |
| Yb | 3.9 | *0.6* | 1.3 | *0.2* | 1.0 | | 0.7 | | 1.2 | *0.01* | 3.2 | *0.5* | 0.7 | *0.1* | 0.8 | *0.2* | 0.7 | *0.1* | 2.8 | *0.3* | 3.39 |
| Lu | 3.3 | *0.2* | 1.0 | *0.1* | 0.7 | *0.2* | 0.5 | *0.1* | 0.8 | *0.3* | 3.0 | *0.2* | 0.4 | *0.1* | 0.7 | *0.4* | 0.4 | *0.02* | 0.4 | *0.1* | 0.503 |
| Hf | 30 | *1.3* | 31 | *1.9* | 29 | *1.9* | 31 | *2.3* | 27 | *4.4* | 29 | *3.0* | 26 | *1.9* | 26 | *1.3* | 24 | *0.5* | 4.1 | *0.3* | 4.84 |
| Ta | 13 | *1.3* | 12 | *0.3* | 12 | *1.0* | 14 | *3.3* | 11 | *0.5* | 11 | *0.7* | 9 | *0.4* | 11 | *2.0* | 7 | *1.3* | 0.5 | *0.1* | 0.78 |
| [d]Pb | 11 | *1.4* | 51 | *2.4* | 47 | *0.8* | 46 | *0.8* | 39 | *2* | 60 | *1.2* | 73 | *2.5* | 71 | *1.4* | 128 | *2.7* | 10 | *0.7* | 11 |
| Th | 17 | *0.9* | 36 | *2.2* | 12 | *1.0* | 18 | *0.2* | 27 | *0.9* | 20 | *1.4* | 23 | *1.6* | 23 | *1.4* | 20 | *0.4* | 5.3 | *0.2* | 5.9 |
| U | 28 | *0.9* | 32 | *1.6* | 26 | *1.8* | 34 | *2.1* | 37 | *0.7* | 36 | *1.0* | 36 | *2.3* | 40 | *1.3* | 36 | *1.2* | 1.6 | *0.1* | 1.69 |
| [e]$Th_N/U_N$ | 0.69 | *0.08* | 1.26 | *0.16* | 0.52 | *0.07* | 0.56 | *0.06* | 0.81 | *0.08* | 0.60 | *0.07* | 0.71 | *0.10* | 0.63 | *0.07* | 0.62 | *0.06* | | | |
| [e]$Th_N/La_N$ | 1.4 | *0.2* | 4.9 | *0.7* | 1.7 | *0.2* | 1.8 | *0.2* | 2.7 | *0.3* | 1.6 | *0.2* | 1.6 | *0.2* | 1.8 | *0.2* | 1.6 | *0.2* | | | |
| [e]$Sm_N/La_N$ | 0.41 | *0.04* | 0.33 | *0.06* | 0.39 | *0.06* | 0.29 | *0.06* | 0.32 | *0.05* | 0.37 | *0.07* | 0.36 | *0.04* | 0.32 | *0.03* | 0.36 | *0.04* | | | |
| [e]$Ce_N/Nb_N$ | 0.67 | *0.07* | 0.46 | *0.07* | 0.60 | *0.06* | 0.58 | *0.12* | 0.67 | *0.10* | 0.97 | *0.10* | 1.33 | *0.15* | 0.96 | *0.11* | 1.40 | *0.22* | | | |

| | | | | | | | | | | | | | | | | | | |
|---|---|---|---|---|---|---|---|---|---|---|---|---|---|---|---|---|---|---|
| [e]$Ce_N/Mn_N$ | 5.8 | *0.5* | 5.0 | *0.6* | 8.2 | *0.8* | 15.6 | *1.8* | 14.7 | *1.2* | 5.7 | *0.5* | 21.7 | *1.9* | 22.2 | *2.0* | 25.7 | *2.0* |
| [e]$Zr_N/Nb_N$ | 1.6 | *0.2* | 1.9 | *0.2* | 2.1 | *0.3* | 1.8 | *0.4* | 1.8 | *0.3* | 2.2 | *0.2* | 2.5 | *0.3* | 1.9 | *0.2* | 2.5 | *0.4* |

[a]The mineral assemblages observed in experimental charges. Allanite was detected as inclusions during LA-ICPMS analysis of quenched melt, the search was not exhaustive. Mineral abbreviations: All, allanite; Ap, apatite; Bi, biotite; Grt, garnet; Ky, kyanite; Phen, phengite; Q, quartz; Rut, rutile; Zir, zircon.
[b]Melt faction estimated from mass balance.
[c]Cl content in melt was from SEM EDS analysis when >0.1 wt%, and from EMP WDS analysis when <0.1 wt%. F content in melt was from EMP WDS analysis.
[d]The bulk Pb content for exp. C3269 is determined to be 18±9.7 ppm, lower than the estimated value (50±10 ppm) for other experiments.
[e]Normalization to the starting composition, e.g., $Th_N/U_N = (Th_{melt}/Th_{EPSM})/(U_{melt}/U_{EPSM})$.
[f]The reference composition for BCR-2G from Jochum and Nohl (2008).

Table 3 Trace element compositions of apatite obtained from regression of LA-ICPMS data.

| Sample | C3269 | | C3922 | | D1222 | | C3927 | | C3955 | | D1218 | | C4049 | | C4058 | | C4059 | |
|---|---|---|---|---|---|---|---|---|---|---|---|---|---|---|---|---|---|---|
| Start. Comp. | EPSM-1 | | EPSM-2 | | EPSM-6 | | EPSM-3 | | EPSM-4 | | EPSM-5 | | EPSM-8 | | EPSM-10 | | EPSM-9 | |
| $^{a}X_{Cl}^{Ap}$ | 0.173 | *0.009* | 0.401 | *0.009* | 0.133 | *0.005* | | | 0.048 | *0.004* | 0.128 | *0.003* | 0.19 | *0.006* | 0.049 | *0.003* | 0.074 | *0.002* |
| $^{a}X_{F}^{Ap}$ | | | | | | | 0.57 | *0.04* | 0.57 | *0.02* | 0.47 | *0.03* | 0.42 | *0.04* | 0.67 | *0.04* | 0.64 | *0.04* |
| ppm | | *σ(10)* | | *σ(10)* | | *σ(8)* | | *σ(13)* | | *σ(10)* | | *σ(7)* | | *σ(9)* | | *σ(18)* | | *σ(4)* |
| Sr | 5072 | *519* | 7071 | *923* | 5436 | *1209* | 4554 | *1053* | 4252 | *1068* | 4449 | *848* | 3151 | *317* | 3796 | *348* | | |
| Y | 202 | *30* | 392 | *14* | 376 | *51* | 338 | *35* | 374 | *25* | 224 | *19* | 234 | *13* | 289 | *18* | 320 | *51* |
| La | 3066 | *28* | 4196 | *158* | 2040 | *49* | 1895 | *63* | 2510 | *129* | 1978 | *57* | 2378 | *93* | 1988 | *62* | 2335 | *250* |
| Ce | 5278 | *83* | 6304 | *255* | 3759 | *57* | 3613 | *127* | 4205 | *206* | 3651 | *115* | 4250 | *108* | 3619 | *123* | 4097 | *65* |
| Pr | 3141 | *50* | 3583 | *153* | 2240 | *55* | 2149 | *80* | 2497 | *121* | 2215 | *86* | 2647 | *98* | 2275 | *64* | 2560 | *95* |
| Nd | 3111 | *84* | 3624 | *143* | 2428 | *95* | 2185 | *94* | 2396 | *97* | 2256 | *107* | 2906 | *86* | 2401 | *93* | 2586 | *362* |
| Sm | 1805 | *37* | 2476 | *80* | 1673 | *153* | 1569 | *96* | 1730 | *43* | 1605 | *70* | 2058 | *75* | 1870 | *63* | 2046 | *227* |
| Eu | 1206 | *14* | 1703 | *57* | 1273 | *61* | 1252 | *59* | 1253 | *27* | 1211 | *49* | 1311 | *36* | 1297 | *54* | 1335 | *179* |
| Gd | 1040 | *43* | 1707 | *60* | 1354 | *103* | 1244 | *88* | 1361 | *37* | 1059 | *42* | 1289 | *37* | 1222 | *47* | 1327 | *226* |
| Dy | 589 | *66* | 1091 | *38* | 939 | *68* | 845 | *73* | 944 | *58* | 730 | *36* | 705 | *30* | 742 | *41* | 780 | *166* |
| Er | 151 | *27* | 307 | *18* | 286 | *37* | 287 | *32* | 308 | *37* | 183 | *30* | 206 | *14* | 239 | *17* | 260 | *54* |
| Yb | 111 | *31* | 166 | *10* | 226 | *53* | 221 | *25* | 251 | *38* | 93 | *14* | 129 | *11* | 161 | *14* | 169 | *50* |
| Lu | 91 | *27* | 126 | *8* | 170 | *31* | 184 | *27* | 209 | *34* | 79 | *17* | 103 | *10* | 131 | *13* | 157 | *41* |
| Th | 227 | *23* | 371 | *78* | | | | | | | 118 | 19 | | | | | 82 | 25 |
| U | 535 | *52* | 587 | *59* | | | | | | | 276 | 50 | | | | | 187 | 86 |
| $^{b}Th_N/U_N$ | 0.5 | *0.1* | 0.7 | *0.2* | | | | | | | 0.5 | 0.1 | | | | | 0.5 | 0.3 |
| $^{b}Th_N/La_N$ | 0.15 | *0.02* | 0.18 | *0.04* | | | | | | | 0.12 | 0.02 | | | | | 0.07 | 0.02 |
| $^{b}Sm_N/La_N$ | 0.60 | *0.05* | 0.61 | *0.06* | 0.84 | *0.10* | 0.85 | *0.09* | 0.71 | *0.07* | 0.83 | *0.08* | 0.89 | *0.09* | 0.96 | *0.09* | 0.90 | *0.16* |
| Mass balance (ppm) | | | | | | | | | | | | | | | | | | |

| | | | | | | | | | |
|---|---|---|---|---|---|---|---|---|---|
| [c]La | 4076 | 3619 | 3918 | 2916 | 2804 | 3062 | 3214 | 2876 | 3033 |
| [c]Ce | 6751 | 5896 | 6301 | 4787 | 4536 | 5023 | 5371 | 4784 | 4974 |
| [c]Th | 1769 | 692 | 1759 | 1227 | 960 | 1270 | 1226 | 1111 | 1230 |

[a]Mole fractions of ClAp and FAp end-members in apatite, obtained from structural formula calculations on the basis of 12.5 $O^{2-}$.
[b]Normalization to the starting composition, e.g., $Th_N/U_N = (Th_{Ap}/Th_{EPSM})/(U_{Ap}/U_{EPSM})$.
[c]La, Ce and Th contents in apatite calculated from mass balance, with the assumption that La, Ce and Th are only hosted by apatite and melt. A large difference between regressed and measured values, especially for Th, indicates the presence of minor allanite in the runs.

Table 4 Trace element partition coefficients between apatite and melt.

| Sample | C3269 | | C3922 | | D1222 | | C3927 | | C3955 | | D1218 | | C4049 | | C4058 | | C4059 | |
|---|---|---|---|---|---|---|---|---|---|---|---|---|---|---|---|---|---|---|
| Start. Comp. | EPSM-1 | | EPSM-2 | | EPSM-6 | | EPSM-3 | | EPSM-4 | | EPSM-5 | | EPSM-8 | | EPSM-10 | | EPSM-9 | |
| | | *σ* | | *σ* | | *σ* | | *σ* | | *σ* | | *σ* | | *σ* | | *σ* | | *σ* |
| La | 126 | *4* | 281 | *23* | 136 | *5* | 95 | *6* | 126 | *11* | 79 | *4* | 83 | *5* | 77 | *4* | 93 | *10* |
| Ce | 173 | *9* | 360 | *42* | 195 | *8* | 153 | *10* | 165 | *10* | 111 | *5* | 113 | *5* | 114 | *7* | 124 | *4* |
| Pr | 210 | *6* | 424 | *51* | 247 | *18* | 209 | *16* | 231 | *13* | 141 | *8* | 146 | *8* | 158 | *6* | 164 | *7* |
| Nd | 263 | *35* | 520 | *28* | 312 | *44* | 258 | *28* | 278 | *41* | 159 | *18* | 193 | *11* | 201 | *12* | 196 | *29* |
| Sm | 186 | *12* | 519 | *69* | 290 | *45* | 283 | *60* | 279 | *34* | 176 | *28* | 202 | *16* | 235 | *16* | 232 | *29* |
| Eu | 92 | *5* | 206 | *18* | 176 | *16* | 165 | *10* | 154 | *6* | 79 | *4* | 82 | *5* | 105 | *9* | 126 | *18* |
| Gd | 146 | *14* | 467 | *133* | 430 | *69* | 357 | *85* | 387 | *123* | 155 | *17* | 216 | *21* | 248 | *20* | 244 | *46* |
| Dy | 79 | *11* | 287 | *14* | 323 | *55* | 333 | *69* | 304 | *19* | 107 | *12* | 202 | *14* | 190 | *17* | 232 | *51* |
| Y | 55 | *12* | 211 | *29* | 287 | *72* | 242 | *67* | 272 | *68* | 66 | *7* | 171 | *24* | 182 | *26* | 238 | *40* |
| Er | 42 | *9* | 167 | *21* | 284 | *83* | 302 | *56* | 330 | *49* | 59 | *11* | 196 | *31* | 212 | *21* | 296 | *66* |
| Yb | 29 | *9* | 123 | *16* | 218 | *51* | 311 | *35* | 217 | *33* | 29 | *6* | 190 | *33* | 203 | *50* | 259 | *90* |
| Lu | 28 | *8* | 122 | *12* | 255 | *82* | 378 | *110* | 278 | *120* | 27 | *6* | 242 | *46* | 179 | *103* | 401 | *108* |
| Sr | 7.9 | *0.8* | 12.1 | *1.6* | 9.1 | *2.1* | 7.6 | *1.8* | 6.9 | *1.7* | 8.4 | *1.6* | 6.3 | *0.7* | 6.4 | *0.6* | | |
| Th | 13 | *1* | 10 | *2* | | | | | | | 6 | *1* | | | | | 4 | *1* |
| U | 19 | *2* | 18 | *2* | | | | | | | 8 | *1* | | | | | 5 | *2* |

Table 5 Fitted parameters for REE partition coefficients between apatite and melt based on the lattice strain model.

| Sample | Data of regression | $D_0$ | σ | E(GPa) | σ | $r_0$(Å) | σ | $R^2$ |
|---|---|---|---|---|---|---|---|---|
| | [a]REE VII | | | | | | | |
| C3269-A | La-Er VII | 226 | *12* | 411 | *64* | 1.184 | *0.004* | 0.972 |
| C3922-A | La-Yb VII | 516 | *19* | 315 | *33* | 1.171 | *0.003* | 0.980 |
| D1222-A | La-Er VII | 365 | *24* | 214 | *58* | 1.140 | *0.006* | 0.907 |
| C3927-A | La-Y VII | 335 | *18* | 273 | *63* | 1.139 | *0.006* | 0.959 |
| C3955-A | La-Y VII | 338 | *21* | 231 | *66* | 1.140 | *0.007* | 0.934 |
| D1218-A | La-Yb VII | 172 | *6* | 354 | *33* | 1.167 | *0.002* | 0.984 |
| | LREE VII | | | | | | | |
| C3922-B | La-Gd VII | 511 | *22* | 233 | *77* | 1.16 | *0.01* | 0.955 |
| C3927-B | La-Gd VII | 374 | *76* | 155 | *102* | 1.11 | *0.05* | 0.983 |
| D1218-B | La-Sm VII | 181 | *17* | 191 | *93* | 1.15 | *0.02* | 0.987 |
| C4049-B | La-Gd VII | 215 | *14* | 215 | *99* | 1.14 | *0.02* | 0.974 |
| C4058-B | La-Gd VII | 249 | *13* | 256 | *85* | 1.14 | *0.01* | 0.988 |
| C4059-B | La-Gd VII | 249 | *18* | 173 | *68* | 1.13 | *0.02* | 0.988 |
| | REE/HREE IX | | | | | | | |
| C3269-C | La-Yb IX | 238 | *9* | 364 | *36* | 1.299 | *0.002* | 0.987 |
| C3922-C | La-Dy IX | 534 | *20* | 259 | *34* | 1.285 | *0.003* | 0.973 |
| D1222-C | La-Yb IX | 309 | *11* | 345 | *76* | 1.289 | *0.005* | 0.988 |
| C3955-C | La-Yb IX | 338 | *20* | 158 | *38* | 1.249 | *0.006* | 0.913 |
| D1218-C | Sm-Lu IX | 178 | *11* | 420 | *117* | 1.27 | *0.01* | 0.990 |
| C4049-C | La-Y IX | 217 | *7* | 187 | *27* | 1.259 | *0.004* | 0.981 |
| C4058-C | La-Y IX | 245 | *5* | 252 | *19* | 1.263 | *0.002* | 0.994 |
| C4059-C | La-Y IX | 247 | *3* | 140 | *12* | 1.245 | *0.003* | 0.997 |
| | LREE IX | | | | | | | |
| C3922-D | La-Sm IX | 528 | *18* | 203 | *63* | 1.28 | *0.01* | 0.987 |
| D1222-D | La-Sm IX | 363 | *22* | 178 | *38* | 1.256 | *0.005* | 0.909 |
| C3927-D | La-Gd IX | 352 | *41* | 134 | *73* | 1.23 | *0.03* | 0.982 |
| D1218-D | La-Sm IX | 176 | *1* | 215 | *14* | 1.275 | *0.002* | 1.000 |
| C4059-D | La-Gd IX | 243 | *3* | 160 | *16* | 1.251 | *0.004* | 0.999 |

[a]Separate regressions were performed for LREE, HREE and all REE data, with VII or IX coordinated REE ionic radii.

Table 6 Results of fitting REE partition coefficients between apatite and melt to the lattice strain model for previous studies: Prowatke and Klemme (2006), Watson and Green (1981), Klemme and Dalpé (2003), Fleet and Pan (1997) and Fleet et al. (2000).

| Sample | Data of regression | $D_0$ | $\sigma$ | $E$(GPa) | $\sigma$ | $r_0$(Å) | $\sigma$ | $R^2$ |
|---|---|---|---|---|---|---|---|---|
| P&K06 | | | | | | | | |
| 78 | [a]Sm-Lu VII | 13.4 | 2.2 | 289 | 90 | 1.193 | 0.020 | 0.999 |
| 77 | La-Lu IX | 26.0 | 2.1 | 274 | 61 | 1.292 | 0.005 | 0.961 |
| 48B | La-Lu VII | 4.8 | 0.3 | 254 | 45 | 1.164 | 0.005 | 0.963 |
| 59B | La-Lu VII | 7.8 | 0.5 | 292 | 54 | 1.165 | 0.004 | 0.964 |
| 43 | La-Lu IX | 17.0 | 1.3 | 222 | 55 | 1.301 | 0.006 | 0.964 |
| W&G81 | | | | | | | | |
| 804ta | REE VII | 5.44 | 0.38 | 241 | 40 | 1.162 | 0.005 | 0.990 |
| 808a | REE VII | 18.93 | 0.86 | 245 | 28 | 1.149 | 0.004 | 0.995 |
| 811b | REE VII | 4.88 | 0.35 | 193 | 38 | 1.159 | 0.006 | 0.986 |
| 812g | REE VII | 40.49 | 0.07 | 234 | 1 | 1.1387 | 0.0002 | 1.000 |
| 814b | REE VII | 9.82 | 0.18 | 230 | 10 | 1.160 | 0.001 | 0.999 |
| 815b | REE VII | 4.74 | 0.46 | 173 | 48 | 1.161 | 0.009 | 0.971 |
| 815a | REE VII | 9.85 | 0.04 | 214 | 2 | 1.1542 | 0.0003 | 1.000 |
| 818b1 | REE VII | 5.46 | 0.03 | 206 | 3 | 1.1689 | 0.0005 | 1.000 |
| 818b2 | REE VII | 5.29 | 0.06 | 198 | 6 | 1.166 | 0.001 | 1.000 |
| 822ta | REE VII | 5.64 | 0.04 | 219 | 4 | 1.155 | 0.001 | 1.000 |
| 823g | REE VII | 18.83 | 0.40 | 221 | 12 | 1.152 | 0.002 | 0.999 |
| | | | | | | | | |
| 808a | REE IX | 18.89 | 0.76 | 215 | 22 | 1.263 | 0.003 | 0.996 |
| 811ta | REE IX | 5.32 | 0.34 | 172 | 30 | 1.269 | 0.006 | 0.988 |
| 812g | REE IX | 40.27 | 0.34 | 204 | 5 | 1.252 | 0.001 | 1.000 |
| 812ta | REE IX | 7.58 | 0.49 | 203 | 32 | 1.274 | 0.005 | 0.990 |
| 814b | REE IX | 9.84 | 0.15 | 202 | 7 | 1.275 | 0.001 | 0.999 |
| 814hh | REE IX | 9.85 | 0.09 | 185 | 4 | 1.273 | 0.001 | 1.000 |
| 814nh | REE IX | 10.74 | 0.48 | 195 | 22 | 1.270 | 0.004 | 0.995 |
| 815b | REE IX | 4.75 | 0.48 | 153 | 44 | 1.275 | 0.009 | 0.969 |
| 818b2 | REE IX | 5.31 | 0.05 | 174 | 4 | 1.280 | 0.001 | 1.000 |
| 818B3 | REE IX | 4.65 | 0.29 | 170 | 28 | 1.274 | 0.005 | 0.989 |
| 822ta | REE IX | 5.64 | 0.06 | 192 | 5 | 1.269 | 0.001 | 1.000 |
| K&D03 | | | | | | | | |
| BS19 | REE VII | 0.56 | 0.02 | 140 | 17 | 1.147 | 0.004 | 0.982 |
| BS19 | REE IX | 0.57 | 0.01 | 121 | 10 | 1.264 | 0.003 | 0.990 |
| BS23 | REE IX | 0.48 | 0.03 | 111 | 27 | 1.247 | 0.008 | 0.944 |
| BS25 | REE IX | 0.47 | 0.05 | 164 | 54 | 1.261 | 0.011 | 0.887 |
| F&P97 | | | | | | | | |
| series D | REE IX | 9.21 | 0.41 | 270 | 36 | 1.300 | 0.003 | 0.982 |
| series D | LREE VII | 6.74 | 0.34 | 267 | 80 | 1.191 | 0.005 | 0.894 |
| series E | LREE VII | 7.67 | 0.03 | 131 | 5 | 1.196 | 0.001 | 0.999 |

| | | | | | | | | |
|---|---|---|---|---|---|---|---|---|
| binary | LREE IX | 3.78 | 0.08 | 115 | 35 | 1.302 | 0.005 | 0.847 |
| Fleet et al. 2000 | | | | | | | | |
| ClAp | REE IX | 0.13 | 0.01 | 159 | 39 | 1.279 | 0.006 | 0.978 |

[a]Separate regressions were performed for LREE, HREE and all REE data, with VII or IX coordinated REE ionic radii.

## Highlights

- Addition of F and Cl in subducted sediment melt results in an increase of LMREE and a decrease of HFSE contents.
- Uptake of LREE, Th, U and Sr in apatite is enhanced by the Cl-Apatite component.
- Apatite-melt partition coefficients for LREE have high values (in the hundreds) for subduction zone *PT* conditions.
- Apatite preferentially incorporates Sm over La, La over U, and U over Th.